



Testing the Strong Equivalence Principle. II. Relating the External Field Effect in Galaxy Rotation Curves to the Large-scale Structure of the Universe

Kyu-Hyun Chae¹, Harry Desmond², Federico Lelli³, Stacy S. McGaugh⁴, and James M. Schombert⁵¹ Department of Physics and Astronomy, Sejong University, 209 Neungdong-ro Gwangjin-gu, Seoul 05006, Republic of Korea; KHC: chae@sejong.ac.kr, kyuhyunchae@gmail.com² Astrophysics, University of Oxford, Denys Wilkinson Building, Keble Road, Oxford, OX1 3RH, UK; HD: harry.desmond@physics.ox.ac.uk³ INAF, Arcetri Astrophysical Observatory, Largo Enrico Fermi 5, I-50125 Florence, Italy; FL: federico.elli@inaf.it⁴ Department of Astronomy, Case Western Reserve University, Cleveland, OH 44106, USA; SSM: ssm69@case.edu⁵ Department of Physics, University of Oregon, Eugene, OR 97403, USA; JMS: schombe@gmail.com

Received 2021 May 17; revised 2021 July 9; accepted 2021 July 29; published 2021 November 5

Abstract

Theories of modified gravity generically violate the strong equivalence principle, so that the internal dynamics of a self-gravitating system in freefall depends on the strength of the external gravitational field (the external field effect). We fit rotation curves (RCs) from the SPARC database with a model inspired by Milgromian dynamics (MOND), which relates the outer shape of an RC to the external Newtonian field from the large-scale baryonic matter distribution through a dimensionless parameter e_N . We obtain a $> 4\sigma$ statistical detection of the external field effect (i.e. $e_N > 0$ on average), confirming previous results. We then locate the SPARC galaxies in the cosmic web of the nearby universe and find a striking contrast in the fitted e_N values for galaxies in underdense versus overdense regions. Galaxies in an underdense region between 22 and 45 Mpc from the celestial axis in the northern sky have RC fits consistent with $e_N \simeq 0$, while those in overdense regions adjacent to the CfA2 Great Wall and the Perseus–Pisces Supercluster return e_N that are a factor of two larger than the median for SPARC galaxies. We also calculate independent estimates of e_N from galaxy survey data and find that they agree with the e_N inferred from the RCs within the uncertainties, the chief uncertainty being the spatial distribution of baryons not contained in galaxies or clusters.

Unified Astronomy Thesaurus concepts: [Non-standard theories of gravity \(1118\)](#); [Modified Newtonian dynamics \(1069\)](#); [Gravitation \(661\)](#); [Disk galaxies \(391\)](#)

Supporting material: machine-readable tables

1. Introduction

General relativity and its Newtonian limit are unique in that the internal gravitational dynamics of a self-gravitating system is unaffected by a constant external gravitational field (Will 2014). This strong equivalence principle (SEP) is generally violated by Milgromian dynamics (MOND; Milgrom 1983), which alters Newton’s laws at low accelerations to explain the dynamics of galaxies without resorting to dark matter (DM). Specifically, MOND violates local position invariance for gravitational experiments because it is nonlinear even in the nonrelativistic regime, so an external acceleration is expected to affect the internal dynamics of a system. This is known as the external field effect (EFE). The most prominent observable consequence of the MOND EFE is that whereas isolated galaxies should have asymptotically flat rotation curves (RCs), galaxies in dense environments should have declining RCs at large radius. Thus, the EFE produces a smoking gun signature of MOND as contrasted with Newtonian dynamics plus DM, as already emphasized in the first paper proposing MOND (Milgrom 1983).

Nonrelativistic field theories of gravity embodying the MOND EFE include the AQUAdratic Lagrangian (AQUAL) theory (Bekenstein & Milgrom 1984) and the quasi-linear MOND (QUMOND) theory (Milgrom 2010). Relativistic theories, which reduce to either AQUAL or QUMOND in the nonrelativistic limit, are under active development (see Famaey & McGaugh 2012;

Milgrom 2014, for reviews). In particular, the proposal of Skordis & Zlošnik (2021) appears particularly promising, as it can reproduce the angular power spectrum of the cosmic microwave background, as well as the linear matter power spectrum.

There have been several attempts to test the EFE empirically (McGaugh & Milgrom 2013a, 2013b; Wu & Kroupa 2015; Hees et al. 2016; Haggi et al. 2016; Famaey et al. 2018), all of which find better agreement with galaxy dynamics when the EFE is included. Recently, Chae et al. (2020b, hereafter Paper I) studied the EFE in 153 rotationally supported galaxies from the Spitzer Photometry and Accurate Rotation Curves (SPARC) database (Lelli et al. 2016). They presented both individual and statistical EFE detections from fitting RCs with an AQUAL-inspired function, which contains the MOND external field strength g_e as a free parameter (see also Chae et al. 2021). They also showed that the median g_e agrees with an independent estimate of the external field strength from the galaxies’ large-scale environments. This is a surprising result from the DM perspective because the observed decline in the RCs occurs well within the tidal radius. Paper I, however, estimated the environmental external fields under the Λ cold dark matter (CDM) paradigm using DM halos as surrogates of the MOND effects; this was expedient because g_e from the large-scale environment cannot be easily computed in AQUAL owing to its nonlinearity.

Here we use a formalism that quantitatively relates the decline of a galaxy’s RC to the strength of the Newtonian external field g_{Ne} at its position. As g_{Ne} is sourced linearly, it can be calculated by summing the Newtonian fields from the large-scale distribution of baryons around the galaxy. Thus, the EFE can be tested directly with the observable Newtonian

external field, and the baryonic content of the nearby universe can be studied as a by-product. The detailed calculation of the Newtonian external gravitational field produced by the baryonic large-scale structure, for direct comparison with the fitted values, is the key advance of this work over Paper I.

In Section 2 we describe our formalism and RC-fitting method, with technical details given in Appendix A. In Section 3 we describe our method for estimating the environmental Newtonian fields, first with an approximate all-sky calculation (Section 3.1) and then with a more detailed calculation within the Sloan Digital Sky Survey (SDSS) footprint (Section 3.2). We present our results in Section 4 and discuss their implications in Section 5. In Appendix B, we provide tables of the fitted parameters and the estimated Newtonian environmental field strengths.

2. Formalism and Fitting Method

Our goal is to infer the external Newtonian field directly from the RCs of galaxies to compare it with the Newtonian field estimated from their cosmic environment, so we need an EFE model that is parameterized by $e_N \equiv g_{Ne}/a_0$, where $a_0 = 1.2 \times 10^{-10} \text{ m s}^{-2}$ is the MOND acceleration scale (McGaugh et al. 2016; Lelli et al. 2017; Li et al. 2018; Chae et al. 2020a; Li et al. 2021). In Paper I we used an AQUAL-based model that was parameterized by $e \equiv g_e/a_0$, where g_e is the MOND external field. In this model, the expected acceleration of a test particle (V^2/R for circular motion) is given by

$$g = \nu_e(g_N/a_0)g_N, \quad (1)$$

where g_N is the Newtonian internal gravitational field (sourced by the galaxy itself) and $\nu_e(y)$ is given by Equation (6) of Paper I with $y \equiv g_N/a_0$ (see also Appendix A). This equation is based on the simple interpolating function (IF; Famaey & Binney 2005; Chae et al. 2019) and the analytic solution of the AQUAL equations in one dimension (Famaey & McGaugh 2012).

In the QUMOND formalism, one can analytically derive the ratio g/g_N as a function of e_N in one dimension. Incidentally, as shown in Appendix A, this ratio is equivalent to Equation (6) of Paper I with $e^2/(1+e) = e_N$ for nonnegative values of e_N . Thus, Equation (1) holds with the replacement of $\nu_e(y)$ with the following:

$$\nu_{e_N}(y) = \frac{1}{2} + \sqrt{\frac{1}{4}D_{e_N}^2(y) + \frac{D_{e_N}(y)}{y}} - \frac{e_N}{\sqrt{|e_N|}} \frac{C_{e_N}}{y}, \quad (2)$$

where $C_{e_N} \equiv \sqrt{1 + |e_N|/4}$ and $D_{e_N}(y) \equiv 1 + |e_N|/y$. Note that $e_N < 0$ is unphysical (similarly to $e < 0$), but we allow it because the measured RCs may prefer negative values empirically. For typical $e_N < 0.01$ and the acceleration range probed by galactic RCs, the last term of Equation (2) mainly controls the EFE and scales almost linearly with $e_N/\sqrt{|e_N|}$. Thus, we define the fitting parameter $\tilde{e} \equiv e_N/\sqrt{|e_N|}$. Our notations are summarized in Table 1.

Values of \tilde{e} for SPARC galaxies may be obtained simply from e of Paper I through an analytically extended transformation such as $\tilde{e} = e/\sqrt{1+e}$ to include negative values. We prefer, however, to obtain values of \tilde{e} directly from fitting Equation (2) to the RCs. Our procedure of obtaining probability density functions (pdf's) of \tilde{e} and galactic parameters is the same as that of Paper I. The galactic parameters are mass-to-light ratio(s) of the disk (and the bulge if present), total gas-to-

Table 1
Summary of Notations

Notation	Meaning
g_{Ne}	Newtonian external field strength
$g_{Ne,fit}$	g_{Ne} from fitting the RC
$g_{Ne,env}$	g_{Ne} from the environment
e_N	g_{Ne}/a_0
$e_{N,fit}$	$g_{Ne,fit}/a_0$
$e_{N,env}$	$g_{Ne,env}/a_0$
\tilde{e}	$e_N/\sqrt{ e_N }$
\tilde{e}_{fit}	$e_{N,fit}/\sqrt{ e_{N,fit} }$
\tilde{e}_{env}	$\sqrt{ e_{N,env} }$

Note. The subscript “fit” or “env” may be dropped when it is obvious from the context. The RC-fitted quantities allow negative values.

hydrogen mass ratio, distance to the galaxy normalized by the SPARC-reported value, and inclination of the disk.

We also revise our selection to maximize the sample size. From the SPARC database of 175 rotationally supported galaxies within distance $D \lesssim 120$ Mpc, the RCs of 163 galaxies have good or acceptable quality ($Q = 1$ or 2). Out of these, 10 galaxies have low measured inclination angles of $< 30^\circ$. Paper I excluded these low-inclination galaxies for their analysis following McGaugh et al. (2016) and thus used only 153 galaxies. Here we use all 163 galaxies, including the low-inclination ones for the purpose of enlarging the sample and since our Markov Chain Monte Carlo (MCMC) procedure allows the inclination angle to vary freely. However, including or excluding low-inclination galaxies does not affect our general results.

Examining all posterior pdf's, we find that for one galaxy (UGC 06787) the pdf is double-peaked and the posterior distance is an order of magnitude larger than the SPARC-reported value ($D = 21 \pm 5$ Mpc). Its RC (from Noordermeer et al. 2007) has an unusual sinusoidal shape that is hard to fit in any context, either with MOND (Li et al. 2018) or with DM halos (Li et al. 2020). The galaxy has a strongly warped HI disk, so the RC shape depends on the details of the warp modeling (the adopted radial variation of position angle and inclination). Considering the unreliable value of the best-fit distance (and probably of \tilde{e}), we drop this galaxy because we aim to compare the external Newtonian field with the location of galaxies on the large-scale structure of the universe. Thus, our analysis is based on a starting sample of 162 SPARC galaxies. As illustrated in Figure 4 of Paper I and discussed further in Appendix B, only RCs that reach very low accelerations can probe the EFE. We select 143 galaxies as described in Appendix B. The fitted \tilde{e} values of these galaxies are compared with the cosmic large-scale structure.

Considering the equivalence of Equations (2) and (A2) with $e/\sqrt{1+e} = \tilde{e}$, we expect the fitted value of \tilde{e} from this work to agree with $e/\sqrt{1+e}$ from Paper I. Figure 1 shows that there is a good match between the two for all galaxies except some at large \tilde{e} .

We stress that our work is not specific to a particular MOND theory because Equation (2) is valid in both AQUAL and QUMOND for the idealized one-dimensional case. In Appendix A, we show that Equation (2) is a good approximation to numerical calculations in the AQUAL context. More generally, Equation (2) can be viewed simply as a fitting function to characterize nonflat outer RCs; then, the extra free parameter e_N is expected to be equal to the external Newtonian

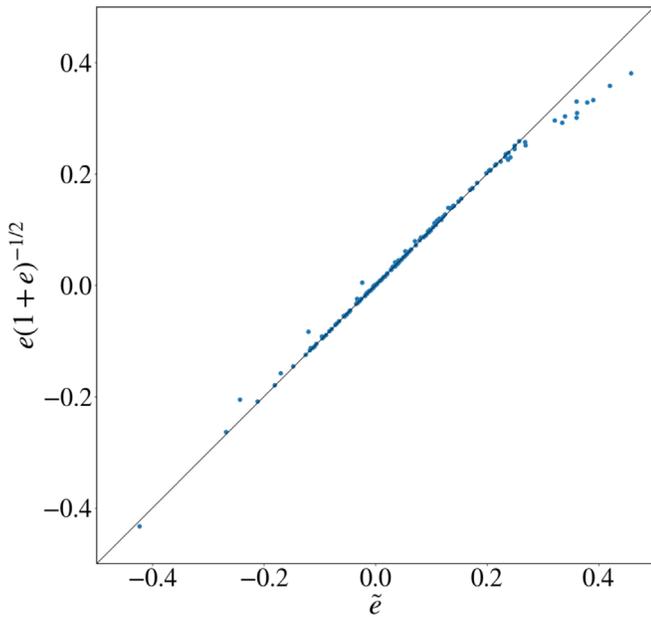


Figure 1. Fitted \tilde{e} values based on Equation (2) from this work are compared with e values based on Equation (A2) from Paper I for 152 overlapping galaxies.

gravitational field (in units of a_0) only if the MOND paradigm is essentially correct.

3. The Newtonian Field from Baryonic Large-scale Structure

We estimate the environmental Newtonian field $g_{\text{Ne,env}}$ by summing the contributions from baryonic mass in various forms in the nearby universe. In MOND, gravitational collapse is expected to become strongly nonlinear at high z (e.g., McGaugh 2015), so the matter power spectrum at $z \simeq 0$ cannot be estimated analytically; one would need large-scale hydrodynamical simulations in a fully fledged MOND cosmology. We therefore compile a census of observed baryonic structures to estimate their Newtonian accelerations directly. We use four main catalogs: the 2M++ galaxy catalog (Lavaux & Hudson 2011), the MCXC galaxy clusters catalog (Piffaretti et al. 2011), the Karachentsev galaxy catalog (Karachentsev et al. 2018; Karachentsev & Kaisina 2019), and the NASA-Sloan Atlas (NSA)⁶ of galaxies. 2M++ and MCXC are used for the approximate all-sky calculation of $g_{\text{Ne,env}}$ (Section 3.1), while MCXC, Karachentsev, and the NSA are used for the more detailed calculation within the SDSS footprint (Section 3.2).

3.1. An All-sky Estimate of $g_{\text{Ne,env}}$

We begin with an approximate all-sky calculation of $g_{\text{Ne,env}}$ to give a sense of its magnitude and investigate its angular variation. This is based primarily on 2M++ (Lavaux & Hudson 2011), an all-sky catalog comprising the Two Micron All Sky Survey (2MASS) Redshift Survey (2MRS), the Six Degree Field Galaxy Redshift Survey Data Release 3 (6dFGRS-DR3), and the SDSS Data Release 7 (DR7). The catalog reaches a depth of $K_S \leq 11.5$ over the full sky and $K_S \leq 12.5$ in the 6dF and SDSS regions. The Galactic plane Zone of Avoidance is populated with mock galaxies by cloning

large-scale structure just outside the Zone to reproduce both one- and two-point statistics of the density field. In view of the approximate nature of this preliminary calculation, we estimate distances from the galaxy’s recession velocity in the rest frame of the cosmic microwave background assuming a Hubble constant of $H_0 = 73 \text{ km s}^{-1} \text{ Mpc}^{-1}$ (as assumed in SPARC; Lelli et al. 2016). We estimate stellar masses assuming a mass-to-light ratio of 0.64 in the K_S band (consistent with 0.5 in the Spitzer [3.6] band as assumed in SPARC; McGaugh & Schombert 2014). We follow the prescription of Lavaux & Hudson (2011) for relating apparent and absolute magnitude. We remove sources with $K_S > 11.5$, which are preferentially seen in the deeper 6dF and SDSS fields, and cut the catalog at 200 Mpc. This leaves 54,483 galaxies out of 69,160 in total.

3.1.1. Adding the Intracluster Medium

We also consider the hot intracluster medium of galaxy clusters. MCXC is a meta-catalog of 1743 X-ray-detected clusters from 12 separate catalogs, many of which derive from the ROSAT satellite (Voges et al. 1999). The catalog provides redshift, coordinates, X-ray luminosity L_{500} in the range 0.1–2.4 keV standardized between component catalogs at a critical overdensity of 500, and the total mass M_{500} . This Λ CDM-based mass is not suitable for our purposes here. In MOND, the mass that sources $g_{\text{Ne,env}}$ is simply the total baryonic mass. The observed baryonic masses of galaxy clusters, however, systematically disagree with the MOND-predicted total masses (from X-ray hydrostatic equilibrium) by a factor ~ 2 (Sanders 1999). Recent X-ray data show a smaller discrepancy (Ettori et al. 2019), but it remains clear that MOND has a missing mass problem in cluster centers. This discrepancy may be driven by undetected baryons (such as very cold gas; e.g., Milgrom 2008), massive sterile neutrinos (Angus et al. 2008), or a gravitating scalar field (Skordis & Zlošnik 2021). In the following, we will estimate the MOND dynamical mass and use it to calculate $g_{\text{Ne,env}}$ regardless of the nature of the missing cluster mass.

We begin with a scaling relation between L_{500} and the observed mass of X-ray-emitting gas (M_X) from an X-ray flux-limited sample of 62 clusters (HIFLUGCS; Zhang et al. 2011):

$$M_X = \frac{10^{14} M_\odot}{E(z)} 10^{(\log(L_{500}/E(z)) - A)/B}, \quad (3)$$

where $A = 44.44$, $B = 1.11$, and $E(z) = 0.3(1+z)^3 + 0.7$. We then build a scaling relation between the observed gas mass and the MOND dynamical mass (M_{MOND}) using the results of the hydrostatic equilibrium analysis of Angus et al. (2008) for 26 X-ray-emitting clusters,

$$\log(M_{\text{MOND}}/M_\odot) = C + D \log(M_X/M_\odot), \quad (4)$$

finding $C = 3.814$ and $D = 0.728$ to provide a good fit to their data.

The results for the clusters’ masses and hence $g_{\text{Ne,env}}$ are not significantly altered if we use the $L_{500} - M_X$ relation of Mantz et al. (2016) instead of Equation (3), or if we use the results of Angus et al. (2008) to convert M_{500} from MCXC directly to M_{MOND} . The latter approach has two disadvantages: (1) it is more sensitive to the Λ CDM-driven choice to measure the mass within a critical overdensity of 500, and (2) it involves an implicit $L_X - M_{500}$ scaling relation assumed by the MCXC team. M_{MOND} is a factor of several lower than M_{500} , so it is important not to use M_{500} directly.

⁶ <https://www.sdss.org/dr13/manga/manga-target-selection/nsa/>

3.1.2. Total Gravitational Field

We calculate $g_{\text{Ne,env}}$ by linearly summing the g_{Ne} values of each of the objects in the combined catalog. For galactic sources—and clusters beyond R_{500} —we treat the sources as point objects because the distances between the source and test points typically greatly exceed the dimensions of the source objects themselves. In case a test point is a distance $d < R_{500}$ from the center of a cluster, we scale the $g_{\text{Ne,env}}$ contribution of the cluster by a factor $(d/R_{500})^3$, i.e., approximating the cluster density as uniform. This does not appreciably affect the results. As our primary interest here is in the angular variation of $g_{\text{Ne,env}}$, we calculate it on a `healpix` (Górski et al. 2005) grid of `nside` = 54 ($\Delta\text{R.A.}, \Delta\text{decl.} \simeq 1^\circ$) every 1.5 Mpc in line-of-sight distance out to 150 Mpc. To remove numerical artifacts, we exclude source objects within 10 kpc of a test point when evaluating $g_{\text{Ne,env}}$ at that point.

As we discuss in detail below, many sources are neglected in this method so that $g_{\text{Ne,env}}$ is underestimated on average. This underestimation is not, however, expected to be a strong function of sky position, so the calculation should be sufficient to estimate the relative variation of $g_{\text{Ne,env}}$ with {R.A., decl.}.

3.2. A More Precise Estimate within the SDSS Footprint

We can calculate $g_{\text{Ne,env}}$ in greater detail within the SDSS footprint, where deeper photometry is available. For this purpose we use the NSA, a value-added catalog based primarily on SDSS data. We calculate $g_{\text{Ne,env}}$ within two regions defined by $\{128 < \text{R.A./deg} < 230, 0 < \text{decl./deg} < 60\}$ and $\{-25 < \text{R.A./deg} < 25, -9 < \text{decl./deg} < 30\}$. We use `ELPETRO_MASS` to estimate stellar mass and `ZDIST` with $H_0 = 73 \text{ km s}^{-1} \text{ Mpc}^{-1}$ to estimate distances. We only cut sources with $D > 500$ Mpc, to ensure that we include sufficient long-range contributions to $g_{\text{Ne,env}}$. The intracluster medium is added in the same way as in Section 3.1.1. In addition, we develop a probabilistic Monte Carlo framework to propagate uncertainties in various input quantities into $g_{\text{Ne,env}}$, as described in more detail below.

In the Local Volume ($D < 11$ Mpc), we replace the NSA with the catalog of Karachentsev et al. (2018), which is complete above a B -band absolute magnitude of about -12 mag and therefore contains fainter galaxies across the sky. It also provides both K -band luminosities and HI masses. We estimate stellar masses from K -band luminosities, again adopting $M/L = 0.64$, and cold gas masses from HI masses using the molecular gas correction of McGaugh et al. (2020):

$$\log(M_{\text{gas}}/M_\odot) = \log(M_{\text{HI}}/M_\odot + 0.07M_*/M_\odot) + \log(1.38). \quad (5)$$

If only an upper limit on M_{HI} is recorded in the catalog, then we estimate it from a scaling relation with M_* (see Section 3.2.2), with a cap at $0.8 M_{\text{HI,max}}$ (this choice does not affect $g_{\text{Ne,env}}$ appreciably). The final Karachentsev catalog contains 1109 galaxies to a sufficiently low mass that a correction for galaxies below the completeness limit is unnecessary.

3.2.1. Adding Galaxies below the SDSS Detection Limit

The SDSS is limited to $m_r < 17.77$ ($m_r < 17.6$ conservatively), so galaxies of increasing stellar mass are progressively absent from the NSA at larger distances. If not corrected for, this would cause the average value of $g_{\text{Ne,env}}$ to fall with distance. To mitigate this selection bias, we add mock galaxies

too faint to be measured by the survey. We use the triple-Schechter fit to the Li & White (2009) stellar mass function (SMF)⁷ to model stellar masses for mock galaxies. In particular, we take 80 logarithmically uniform bins in stellar mass M_* between 10^5 and $10^{13} M_\odot$ and 50 linear bins in distance D between 11 and 500 Mpc. In each $\{M_*, D\}$ bin we use the SMF to calculate the expected number of galaxies. We then assign absolute r -band magnitudes to these mock galaxies using the scaling relation

$$M_r = E \log(M_*/M_\odot) + F, \quad (6)$$

with $E = -1.991$, $F = -0.265$, and a Gaussian scatter in M_r of 0.385 dex, fitted directly from the NSA data, and convert to apparent magnitude in the same manner as for 2M++. We conservatively consider the galaxies visible to SDSS to be those with $m_r < 17.6$. This lets us calculate the average fraction of the total stellar mass that is included in each radial bin when using the NSA catalog directly; the remaining mass must now be added back in so that $g_{\text{Ne,env}}$ is not biased low at large D . Ideally a similar completeness correction would be applied to the galaxy cluster catalog. We do not attempt this here because the cluster mass function is not well characterized, but note that the higher intrinsic brightness of galaxy clusters makes them visible to much larger distances than individual galaxies, so we expect the problem to be less severe.

While the above calculates the one-point function of the missing mass, its two-point function (i.e., clustering) is also relevant to the $g_{\text{Ne,env}}$ that it produces. To model this, we consider the two most extreme scenarios: we assume either that the mock galaxies are randomly distributed in space within each distance annulus (i.e., unclustered) or that they are satellites of the galaxies included in the NSA so that they may be considered coincident with them (i.e., maximum clustering). These models bracket the full range of possible clustering strengths; we will refer to them as the “no clustering” and “max clustering” models, respectively.

For the “max clustering” method we multiply the mass of each NSA galaxy by the reciprocal of the mass fraction calculated above for the corresponding distance bin, so that the correct total amount of mass is modeled in each bin. For the “no clustering” method we explicitly add mock galaxies with $m_r > 17.6$ to our source catalog before calculating $g_{\text{Ne,env}}$; this is done separately for each mass and distance bin described above, and the galaxies are given random positions within the bin. This primarily increases the uncertainty in $g_{\text{Ne,env}}$ when the random positions of the mock galaxies are marginalized over by Monte Carlo sampling, while the “max clustering” method primarily boosts $g_{\text{Ne,env}}$. We find this boost to $g_{\text{Ne,env}}$ to be ~ 0.1 dex, and hence not negligible. On the other hand, altering the widths of the mass or distance bins, the functional form of the SMF (within reasonable limits), or the minimum stellar mass down to which mock galaxies are included has a negligible effect on the results. Note that these methods for adding undetected galaxies preserve any over- or under-densities in galaxy number counts within the NSA as a function of distance, allowing them to manifest as a distance or other environment dependence of $g_{\text{Ne,env}}$.

⁷ This agrees well with the elliptical Petrosian SMF of the NSA (Stiskalek et al. 2021).

3.2.2. Adding Gas to Galaxies

Galaxies contain an appreciable amount of gas, either “cold” ($T \lesssim 10^4$ K) gas, residing in star-forming atomic or molecular disks, or “hot” ($T \gtrsim 10^5$ K) gas, residing in X-ray-emitting ionized halos. The gas content depends on both stellar mass and morphology, with low-mass late-type galaxies having a larger fraction of cold gas and high-mass early-type galaxies having a larger fraction of hot gas.

To model the gas content of our source galaxies, we begin by estimating the galaxy type as a function of its stellar mass. From Henriques et al. (2015), the early-type fraction is given by $f_{\text{early}} \simeq 0.28 \log(M_*/M_\odot) - 2.12$. We use this as a probability to assign an early-type or late-type flag to each source galaxy, separately within each Monte Carlo realization of the model so that the uncertainty it induces is naturally propagated into $g_{\text{Ne,env}}$. For late-type galaxies, the gas mass is given by

$$M_{\text{g,cold}} = 11,500 (M_*/M_\odot)^{0.54} + 0.07 M_*, \quad (7)$$

where the first and second terms in the sum consider, respectively, atomic (Lelli et al. 2016) and molecular (McGaugh et al. 2020) gas. For early-type galaxies, the gas mass is instead given by

$$\log(M_{\text{g,hot}}/M_\odot) = 1.47 \log(M_*/M_\odot) - 5.414. \quad (8)$$

We derived this scaling relation considering 94 early-type galaxies with hot gas masses from the Chandra X-ray observatory (Babyk et al. 2018) and stellar masses from our own WISE photometry (following the same procedures as in Lelli et al. 2016), adopting $M_*/L_{\text{W1}} = 0.7$ as appropriate for early-type galaxies (Schombert et al. 2019). We take a scatter in both $\log(M_{\text{g,cold}}/M_\odot)$ and $\log(M_{\text{g,hot}}/M_\odot)$ of 0.2 dex and add gas masses in the same way to the faint mock galaxies of Section 3.2.1.

3.2.3. Adding Baryonic Mass outside the SDSS Footprint

Thus far, our catalog of $g_{\text{Ne,env}}$ sources is all-sky within 11 Mpc but restricted to the SDSS footprint beyond that. Since gravity is a long-range force, this will lead to an underestimation of $g_{\text{Ne,env}}$ on average at $D > 11$ Mpc and a spurious dependence of $g_{\text{Ne,env}}$ and its direction on sky position within the NSA footprint. To mitigate this effect, we add a uniform grid of mass outside the SDSS footprint out to 500 Mpc. We calculate the density of this grid by integrating the SMF over all masses, including the corrections for cold and hot gas as a function of stellar mass as described above, as well as adding in the average density of cluster mass. This gives $\rho_{\text{tot}} = 10^{8.549} M_\odot \text{Mpc}^{-3}$. We use a Cartesian grid of spacing 5 Mpc in each direction, so that each grid cell has a mass of $4.4 \times 10^{10} M_\odot$. To soften its g_{Ne} contribution, we assume this mass to have a spherical Gaussian density profile with width $\sigma = 1.25$ Mpc, so that the gravitational field it sources at a displacement \mathbf{r} from its center is

$$g_{\text{N}}(\mathbf{r}) = -\frac{GM}{r^2} \left(\text{erf}\left(\frac{r}{\sqrt{2}\sigma}\right) - \sqrt{\frac{2}{\pi}} \frac{r}{\sigma} \exp\left(-\frac{r^2}{2\sigma^2}\right) \right) \hat{r}. \quad (9)$$

This can have a ~ 0.2 dex effect on $g_{\text{Ne,env}}$ and tends to reduce variation in $g_{\text{Ne,env}}$ with distance owing to the homogeneity of the grid mass. The result is not significantly altered if the grid

spacing is reduced to 2.5 Mpc, if the SMF of Li & White (2009) is replaced by that of Moffett et al. (2016) or Bernardi et al. (2013), or if the grid cells are uniformly spaced in D^2 rather than D so that finer structure is resolved at smaller D . This indicates that the manner in which mass is distributed outside the SDSS footprint is not critical for the gravitational field within it, although it is important that the correct mass on average is modeled.

3.2.4. Adding Cosmological Missing Baryons

The above method accounts for baryons in each of the forms in which they are readily visible: stars, cold and hot gas in galaxies, and an X-ray-emitting intracluster medium. However, there may be “missing baryons” not found in one of these forms. This is a necessity in Λ CDM, where Ω_b is known precisely from the cosmic microwave background but found to be much larger than that implied by a census of visible mass locally (e.g., Shull et al. 2018). The result for Ω_b is likely to hold in a MOND cosmology as well, where at early times (e.g., during big bang nucleosynthesis) the high average density of the universe makes the MOND modification to gravity ineffective. This is, however, subject to the considerable uncertainty in MOND cosmology, stemming largely from the unknown relativistic parent theory; see, e.g., Famaey & McGaugh (2012). In the case of the relativistic MOND theory of Skordis & Zlošnik (2021), we expect big bang nucleosynthesis to work in MOND in nearly the same way as in Λ CDM, so the missing baryons problem should be analogous in both cosmologies.

We adopt the census of baryons from Shull et al. (2018), who find that baryons in the forms we explicitly model amount to $\sim \Omega_b/8$ (with $\Omega_b \simeq 0.046$; Macquart et al. 2020), meaning that there are potentially $\sim 8\times$ more baryons than we have included so far. As an additional consistency check on our mass model, we calculate that it produces total densities of all baryonic components within the SDSS footprint that are approximately consistent with the results of Shull et al. (2018). Similarly to our method for adding faint galaxies, we consider two extreme clustering models for these missing baryons: (1) they are completely unclustered (or equivalently nonexistent) and so do not alter $g_{\text{Ne,env}}$, or (2) they are maximally clustered with the structures we model and equally distributed between them, causing a uniform increase in the magnitude of the $g_{\text{Ne,env}}$ field by a factor of 8.

Our assumption is that the cosmological missing baryons are too far from the centers of galaxies and clusters to appreciably alter their measured kinematics. This is reasonable even for the “max clustering” model because the scales involved in calculating $g_{\text{Ne,env}}$ ($\gtrsim 10$ Mpc) are much larger than those over which kinematics can be probed (< 1 Mpc). These missing baryons are therefore fully independent of those potentially invoked in Section 3.1.1 to explain the dynamical masses of clusters. Nevertheless, it is possible that the potential missing baryons inside clusters may account for some fraction of the cosmological missing baryons, leading us to overestimate $g_{\text{Ne,env}}$ when multiplying by a factor of 8. This effect is, however, small ($\sim 10\%$), and the “max clustering” model is intended to give an upper bound on plausible $g_{\text{Ne,env}}$ values, so that it brackets the possible range along with the “no clustering” model. In fact, the difference between M_X and M_{MOND} in clusters may be due to neutrinos or a massive scalar field rather than dark baryons.

3.2.5. Modeling Uncertainties

Finally, it is important to estimate the uncertainty in $g_{\text{Ne,env}}$ due to uncertainties in our baryonic mass model of the universe. This includes uncertainties in the scaling relations that we use to determine gas and cluster masses, the locations of mock galaxies above the magnitude limit of SDSS, and the basic properties of the source objects themselves (e.g., distances and stellar masses). Our Monte Carlo framework makes it easy to propagate these uncertainties: at each test point we evaluate $g_{\text{Ne,env}}$ 2000 times, in each case randomly sampling from the distributions describing the input variables. This is a sufficient number for convergence of the $g_{\text{Ne,env}}$ pdf's.

We use a 30% uncertainty in M_* and M_{MOND} , describing uncertainties in stellar mass-to-light ratios and the calculation of the MOND dynamical mass of galaxy clusters. We use a 0.2 dex scatter in cold and hot gas masses of galaxies and 0.4 dex in cluster masses to account for the additional uncertainty in the conversion from X-ray luminosity to hot gas mass. Following Lelli et al. (2016), distance uncertainties are based on the following scheme (suitable for Hubble-flow distances): 30% for $D < 20$ Mpc, 25% for $20 \leq D/\text{Mpc} < 40$, 20% for $40 \leq D/\text{Mpc} < 60$, 15% for $60 \leq D/\text{Mpc} < 80$, and 10% for $D > 80$ Mpc.

The remaining uncertainties derive from the assignment of an early-type/late-type flag to each galaxy and the distribution of faint mock galaxies within each distance bin in the “no clustering” model for filling in faint galaxies. We note that the “no clustering” model for cosmic missing baryons is different from that for faint mock galaxies in that it does not discretize the missing mass and assign it a random position. The uncertainty induced by cosmic missing baryons is therefore entirely in the systematic difference between the “no clustering” and “max clustering” models. We summarize the resulting $g_{\text{Ne,env}}$ distribution over all Monte Carlo realizations at each test point by its mean and standard deviation.

We evaluate $g_{\text{Ne,env}}$ at the positions of the Karachentsev and NSA galaxies themselves out to 150 Mpc to assess its trend with environment and distance, and at the positions of the SPARC galaxies for a direct comparison with $g_{\text{Ne,fit}}$. We exclude from the source catalog the test galaxy under consideration, either by simply masking out the corresponding galaxy from the source array (for a Karachentsev or NSA galaxy) or, for a SPARC galaxy, by using NED to determine whether it is in the NSA and an R.A./decl. match with tolerance 0.1 deg to determine whether it is in the Karachentsev catalog.

4. Results

4.1. Qualitative Consistency with Large-scale Structure

We consider a cylindrical space of radius $R = 150$ Mpc and height $Z = 50$ Mpc in the northern sky (decl. $\delta > 0^\circ$), where the vast majority of fitted galaxies (126) are located. In Figure 2, the SPARC galaxies are projected on the equatorial plane of this cylindrical space, together with galaxies from the 2M++ catalog (Lavaux & Hudson 2011). At $22 \lesssim R/\text{Mpc} \lesssim 45$, there is an underdense region in which SPARC galaxies tend to give lower $\bar{\epsilon}$ values than the median. At $45 \lesssim R/\text{Mpc} \lesssim 100$, instead, there are two massive structures: the CfA2 Great Wall (Geller & Huchra 1989) toward R.A. $\alpha \simeq 180^\circ$ and the Perseus–Pisces Supercluster (Joeveer & Einasto 1978) toward $\alpha \simeq 45^\circ$. Several SPARC galaxies are located in these overdense structures and tend to give a higher $\bar{\epsilon}$ value than

the median. This seems qualitatively consistent with an EFE interpretation of the $\bar{\epsilon}$ values from RC fits. The situation is more complex at $R < 22$ Mpc owing to a finger-like structure toward $\alpha = 190^\circ$, which varies with height and disappears at $Z > 11$ Mpc. The precise geometry of this structure may affect the $\bar{\epsilon}$ values in a way that cannot be simply inferred by looking at projected maps. However, note that the two “golden galaxies” NGC 5033 and NGC 5055 highlighted in Paper I are near the Virgo Supercluster, while the control galaxy NGC 6674 is in the underdense ring. The other control galaxy NGC 1090 is in the southern sky, so it is not included in Figure 2.

Figure 3 shows the distribution of $\bar{\epsilon}$ versus cylindrical radius R for the 126 SPARC galaxies within the cylindrical space. It is evident that galaxies in the underdense region at $22 \text{ Mpc} < R < 45 \text{ Mpc}$ have low values of $\bar{\epsilon}$ consistent with zero environmental fields. The median value within this radial bin is $0.016_{-0.027}^{+0.015}$ (with bootstrap uncertainties), thus consistent with no-EFE detection as expected from the large-scale distribution of galaxies. On the other hand, galaxies in a radial bin at $R > 45$ Mpc, in which the CfA2 Great Wall and the Perseus–Pisces Supercluster are located, display a median value of $\bar{\epsilon} = 0.103_{-0.008}^{+0.030}$, significantly different from zero at $\sim 13\sigma$. This shows a striking contrast with the middle bin. The majority of the galaxies in the third bin, indeed, are associated with the CfA2 Great Wall or the Perseus–Pisces Supercluster.

These results demonstrate qualitative consistency between the Newtonian external field inferred from galactic RCs and the large-scale galaxy distribution. To make a more detailed comparison, Figure 4 shows a full-sky Mollweide projection of the mean environmental field $g_{\text{Ne,env}}$ from the 2M++ plus MCXC calculation (Section 3.1) over different distance bins: $0 < D/\text{Mpc} < 11$, $11 < D/\text{Mpc} < 30$, $30 < D/\text{Mpc} < 60$, and $60 < D/\text{Mpc} < 120$. These are chosen to represent (1) the Local Volume, (2) the remainder of the overdense region we identify in the SDSS footprint (see Section 4.2), (3) the underdense region farther out, and (4) the CfA2 Great Wall and the Perseus–Pisces Supercluster regions. Note that here we use three-dimensional distance D from the Milky Way, rather than cylindrical radius R , to provide an alternative perspective. Again we find qualitative agreement between the RC-fitted field $g_{\text{Ne,fit}}$ and the environmental field $g_{\text{Ne,env}}$ in terms of their spatial variations. In particular, the Local Void (Tully et al. 2019) is clearly visible as the blue regions with low values of $g_{\text{Ne,env}}$ at $D < 11$ Mpc; galaxies within the void tend to have values of $g_{\text{Ne,fit}}$ below the average, as expected.

4.2. Quantitative Comparison in the SDSS Footprint

We now consider a quantitative comparison of $\bar{\epsilon}$ with the environmental field estimated in Section 3.2. To begin, we calculate $g_{\text{Ne,env}}$ at the positions of the Karachentsev and NSA galaxies themselves out to 150 Mpc. This provides a fair tracing of the gravitational field over the nearby large-scale structure. Figure 5 plots the mean $g_{\text{Ne,env}}$ values as a function of distance. We use here the “max clustering” model, which we will find below to match the fitted values better than the “no clustering” case, although the qualitative trends are the same. We see that $g_{\text{Ne,env}}$ falls from $D = 0$ to $D \simeq 50$ Mpc and then rises again out to ~ 100 Mpc before leveling off. For both $D < 40$ Mpc and $80 < D/\text{Mpc} < 120$, $g_{\text{Ne,env}}$ is significantly larger toward $\alpha \simeq 180^\circ$ than elsewhere, indicating excess structure in that direction. This is largely due to the Virgo Cluster at small distance and the CfA2 Great Wall at $D \simeq 100$

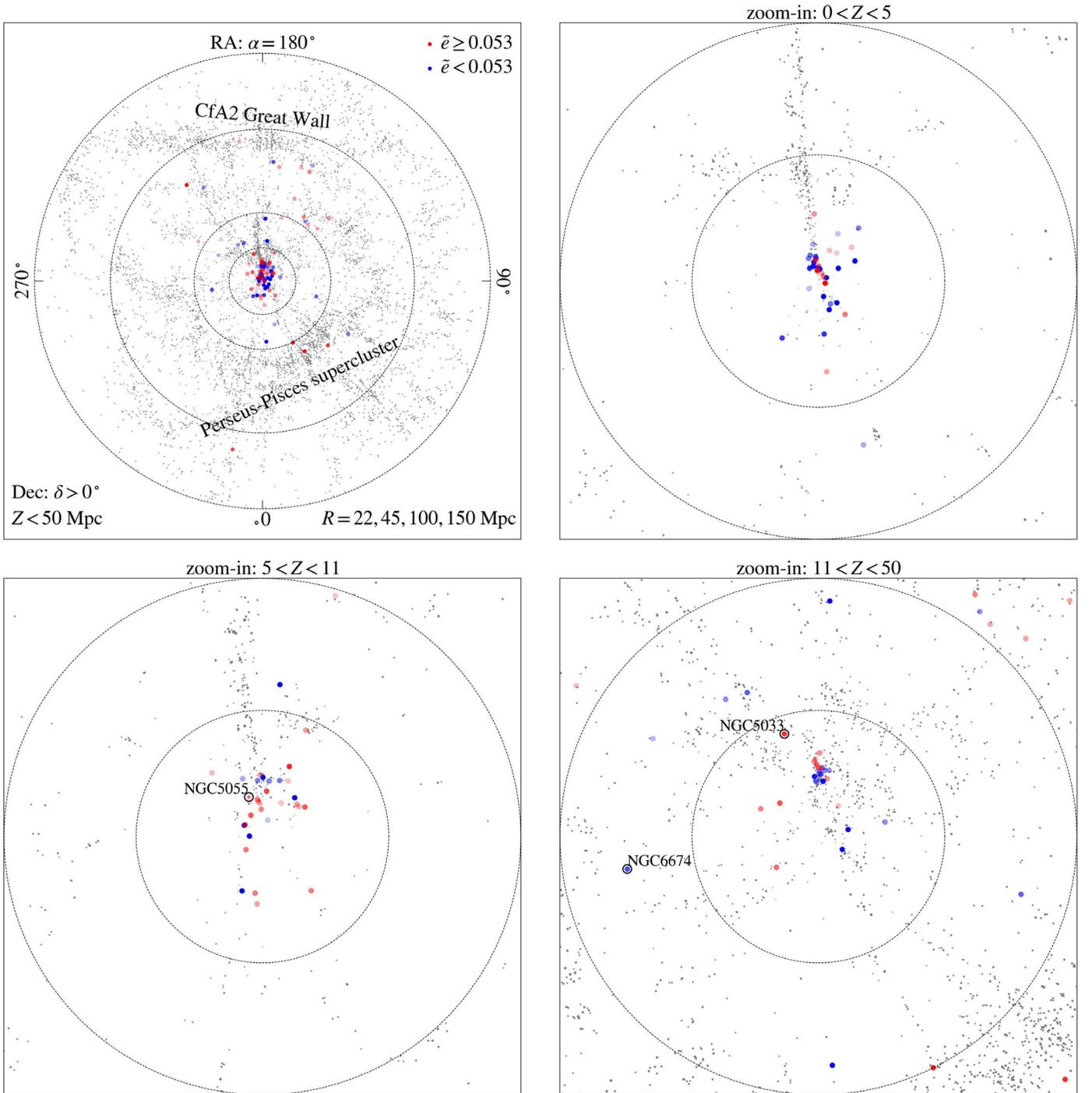


Figure 2. The top left panel shows a map of galaxies in a cylindrical space of the northern sky with a radius of 150 Mpc and a height of 50 Mpc. Galaxies are taken from the 2M++ catalog (accepting only those brighter than 11.5 in K -magnitude to prevent any direction bias), and the area of each point is proportional to the stellar mass of the galaxy. SPARC galaxies with external Newtonian fields from RC fits are indicated by colored points. External Newtonian fields higher and lower than the median ($\bar{e} = 0.053$) are shown in red and blue, respectively, and the opacity of the point is proportional to $|\bar{e} - 0.053|/(\text{uncertainty of } \bar{e})$. The central $R < 45$ Mpc region is sliced and zoomed-in in the other panels. These panels show an overdensity–underdensity contrast in the two opposite directions of R.A. $\alpha = 180^\circ$ and 0° . Two “golden” galaxies and one control galaxy from Paper I are indicated. The first ring-like region with $R = (22, 45)$ Mpc is relatively underdense, and the fitted \bar{e} values are mostly lower in this region. The second ring-like region of $R = (45, 100)$ Mpc includes the Cfa2 Great Wall and the Perseus–Pisces Supercluster. The fitted \bar{e} values are mostly higher in this region.

Mpc. The part of the SDSS footprint in the Southern Galactic Cap ($-25^\circ < \alpha < 25^\circ$, $-9^\circ < \delta < 30^\circ$) has a weaker field on the whole, especially at $D \simeq 20$ Mpc, where it can be seen as a disjoint band of low- $g_{\text{Ne,env}}$ points. Very similar trends are seen if the distance D is replaced by the cylindrical distance R adopted in Figures 2 and 3.

We now evaluate $g_{\text{Ne,env}}$ at the positions of the SPARC galaxies. Restricting to the SDSS footprint retains 109 SPARC galaxies, although only 90 of these have a measured \bar{e} satisfying the cut $x_{0,3} < -10.6$. Figure 6 shows $\log(e_{\text{Ne,env}})$ for the SPARC galaxies as a function of distance, including their full uncertainties, for both the “no clustering” and “max

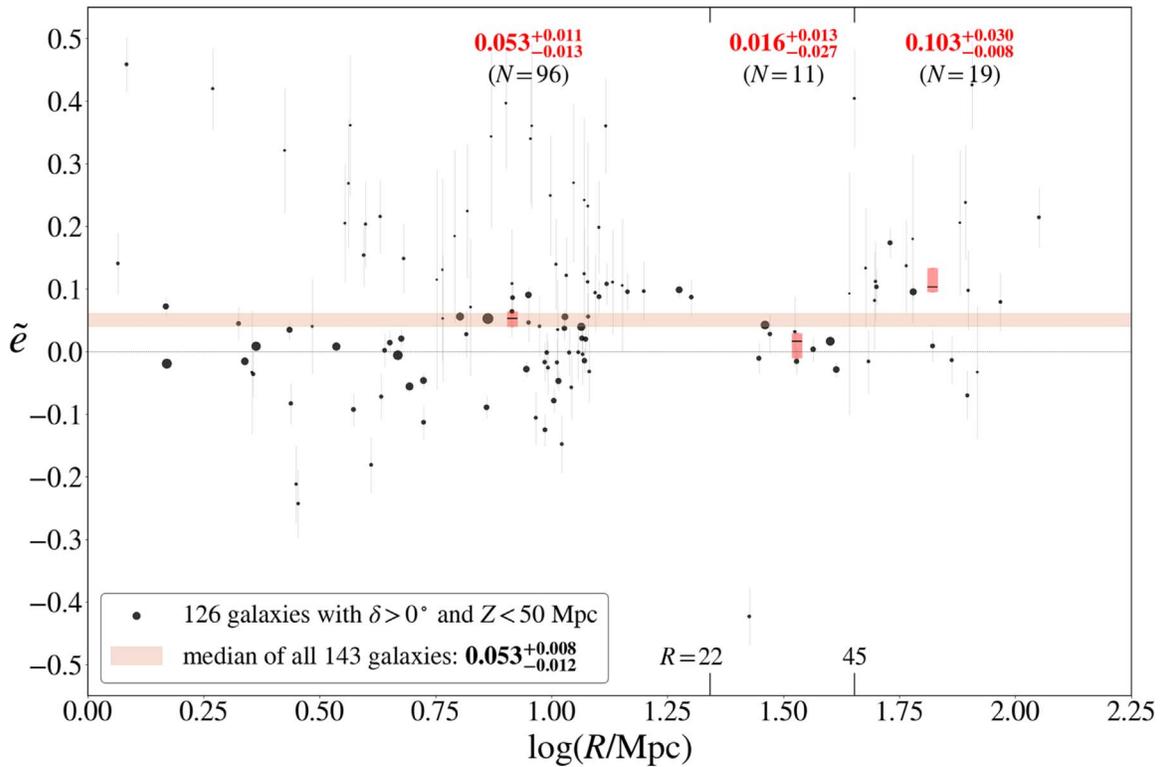


Figure 3. RC-fitted values of \tilde{e} vs. the cylindrical radius defined in Figure 2 for 126 SPARC galaxies in the northern hemisphere. The size of a dot is inversely proportional to the uncertainty on \tilde{e} . The light-red band shows the median value and its uncertainty for all galaxies shown in Figure 12. The red bars show median values (black line) and their uncertainties in three radial bins. The number of galaxies in each radial bin and their median values with bootstrap 1σ uncertainties are indicated at the top. \tilde{e} is systematically lower in the underdense second bin and higher in the third bin.

clustering” models. Although the statistical uncertainties are considerable, the distance trend is still clearly visible, as is the factor ~ 8 difference between the two clustering models driven by the influence of baryons not found in stars, cold gas, or the intracluster medium.

Figure 7 exhibits individual values of \tilde{e}_{fit} against \tilde{e}_{env} for the sample of 90 SPARC galaxies as a function of distance. Remarkably, the median value of \tilde{e}_{fit} from rotation-curve fits is well within the allowed values from the two clustering models. This is highly nontrivial because, in a general DM context, \tilde{e} is merely a fitting parameter to describe the outer shapes of RCs. It could have taken a value across orders of magnitude, so there is no a priori reason why its median value should lie within the boundaries of the \tilde{e}_{env} calculation from the large-scale distribution of baryonic matter. Moreover, both \tilde{e}_{fit} and \tilde{e}_{env} are lower than average in the underdense region $30 < D/\text{Mpc} < 60$ while clearly higher than average in the overdense region $D > 60$ Mpc, consistent with the trend of \tilde{e}_{fit} for all 126 galaxies within $Z < 50$ Mpc in the northern sky shown in Figure 3.

To check the agreement between \tilde{e}_{fit} and \tilde{e}_{env} in more detail, Figure 8 shows the distribution of their differences. Remarkably, there is an excellent statistical match between \tilde{e}_{fit} and \tilde{e}_{env} of the “max clustering” case, while there is some tension with the “no clustering” case. This result suggests that accounting for missing baryons is important in MOND. Moreover, it agrees with previous indications that the missing baryons are likely significantly correlated with galaxies and groups (e.g., Nicastro et al. 2018; Das et al. 2019, 2020; Lim et al. 2020).

Finally, we check directly the correlation between \tilde{e}_{env} and \tilde{e}_{fit} for the sample of 90 galaxies shown in Figures 7 and 8 using

Pearson’s linear correlation coefficient r . Because \tilde{e}_{fit} has a large uncertainty ranging from 0.004 to 0.194 with a median value of 0.047 for these galaxies, we expect the correlation to be weak. In Figure 9 we compare the measured correlation coefficient with the expected distribution from a Monte Carlo simulation. This simulation assumes that $\tilde{e}_{\text{fit}} = \tilde{e}_{\text{env}}$ fundamentally, with \tilde{e}_{fit} scattered by the error budgets of both quantities. For \tilde{e}_{env} we use the mean of the “max clustering” and “no clustering” values. For the uncertainty of \tilde{e}_{env} , we take the average of the statistical errors of the “max clustering” and “no clustering” cases for the statistical error and one-half of the difference between the “max clustering” and “no clustering” cases for the systematic error. For the uncertainty of \tilde{e}_{fit} , we take the measured values (see Appendix B) for the statistical error and 0.02 for the systematic error of our model (see Section A.2). These errors are added in quadrature for each galaxy, with the result used to scatter \tilde{e}_{fit} in each Monte Carlo realization.

We find the measured coefficient of $r = 0.057$ to agree well with the distribution from the mock data, with a 27% probability of a lower r under the hypothesis $\tilde{e}_{\text{fit}} = \tilde{e}_{\text{env}}$. The mock data have an rms scatter of 0.077 ± 0.008 for \tilde{e}_{fit} . This is about 3/5 of the measured scatter for this sample, indicating that the uncertainties of \tilde{e}_{fit} and/or \tilde{e}_{env} may be somewhat underestimated. Regardless of the precise error model, it is clear that the theoretically expected correlation between \tilde{e}_{fit} and \tilde{e}_{env} values of individual galaxies cannot be directly inferred given the current observational uncertainties. The existing data, however, are consistent with the existence of an intrinsic correlation between \tilde{e}_{fit} and \tilde{e}_{env} .

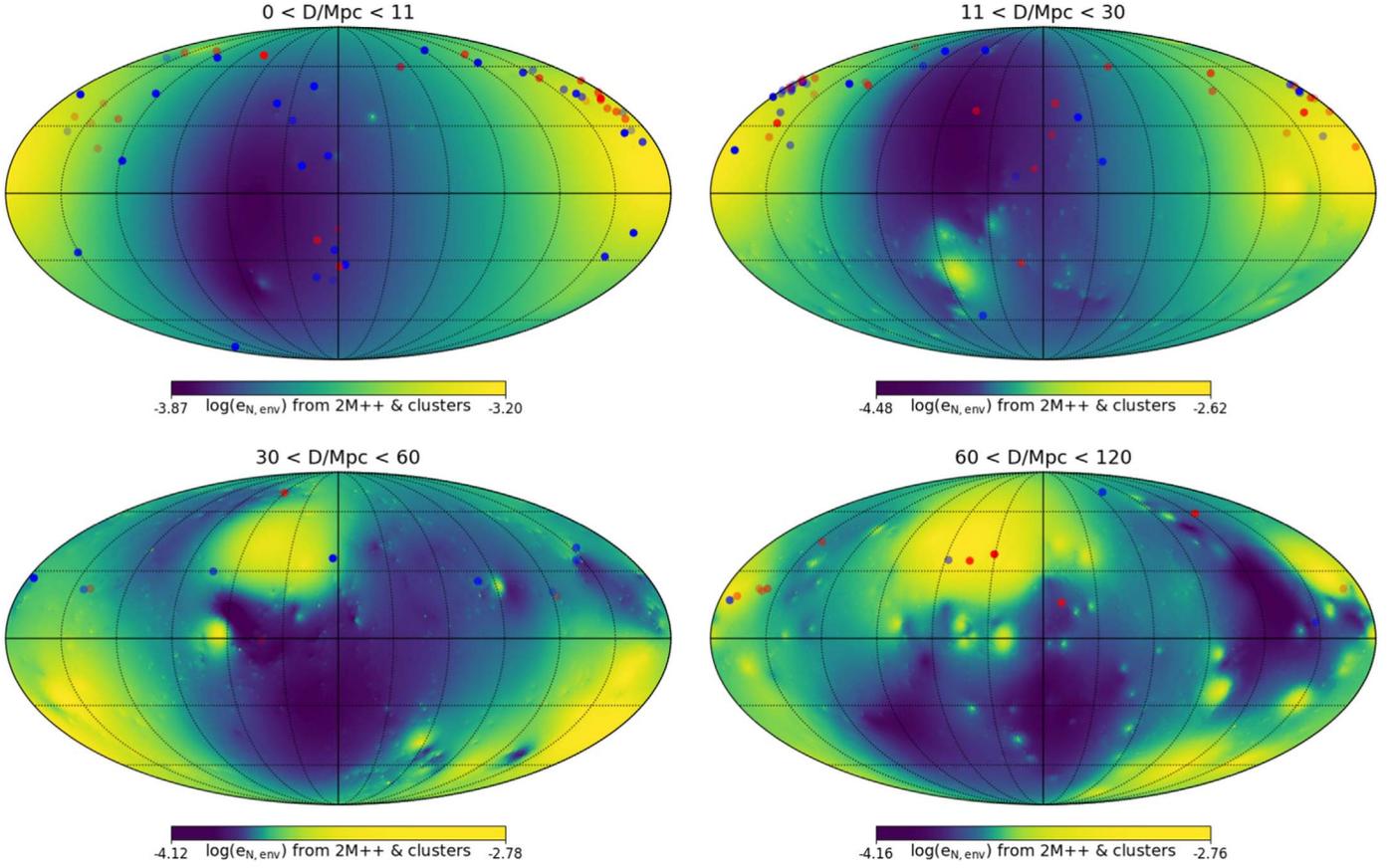


Figure 4. All-sky distributions of the environmental field $g_{Nc,env}$ from 2M++ galaxies and MCXC clusters in Mollweide projection and equatorial coordinates averaged across various distance ranges. The locations of SPARC galaxies with independent estimates of g_{Nc} from RC fits are shown: red and blue points indicate $\bar{z}_{fit} \geq 0.053$ and $\bar{z}_{fit} < 0.053$, respectively; the opacity of the point increases with $|\bar{z}_{fit} - 0.053| / (\text{uncertainty in } \bar{z}_{fit})$ as in Figure 2.

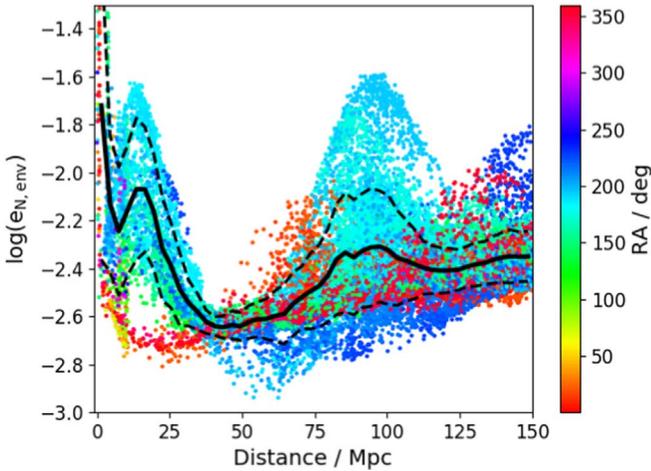


Figure 5. Variation of $e_{N,env}$ with distance for the galaxies in the NSA and Karachentsev catalogs. Individual galaxies are color-coded by right ascension (R.A.). The black lines show the mean trend (solid) and standard deviation (dashed) in bins of distance. This plot assumes the “max clustering” model for the missing baryons (see Figure 6).

5. Discussion and Conclusion

Using a simple, generic fitting function (Equation 2), we investigate the EFE in the RCs of 143 SPARC galaxies, using a dimensionless parameter \bar{z} related to the external Newtonian gravitational field. We find that \bar{z} is well correlated with the observed large-scale structure of baryonic mass distribution

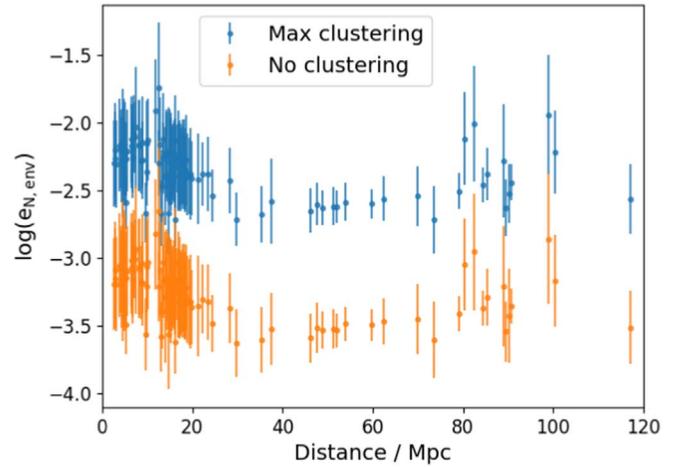


Figure 6. Variation of $e_{N,env}$ with distance for the SPARC galaxies within the NSA footprint. The “max clustering” model (blue) assumes that missing baryons are effectively coincident with observed structures, while the “no clustering” model (orange) distributes them uniformly in space. See Section 3.2.1 for details.

(Figure 2). The fitted values are consistent with zero in an underdense ring region at cylindrical radii $22 \text{ Mpc} < R < 45 \text{ Mpc}$, while they are a factor of two higher than the average external field at or near the CfA2 Great Wall and the Perseus–Pisces Supercluster (Figure 3). In this high-density region the EFE is statistically detected at $\sim 13\sigma$. The correlation between \bar{z}_{fit} and

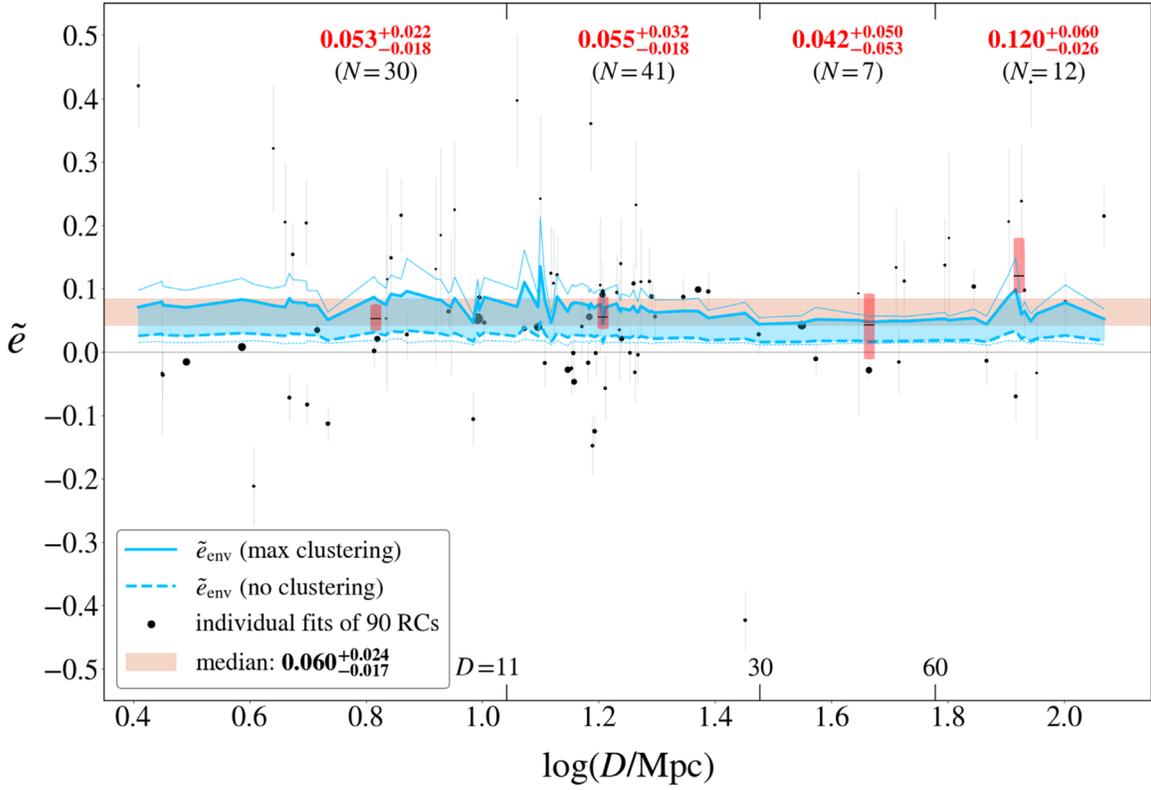


Figure 7. The external Newtonian gravitational fields from RC fits (dots with error bars), parameterized by \tilde{e} , are compared with those from the large-scale distribution of baryonic matter (blue band) as a function of distance to 90 SPARC galaxies that probe the low-acceleration regime and are within the SDSS footprint. The size of each black dot is inversely proportional to its statistical uncertainty. The median value of \tilde{e}_{fit} and the associated uncertainty are represented by the light-salmon band. The medians and associated bootstrap uncertainties in four distance bins are shown by red bars, with the values indicated at the top. The blue band is obtained considering the “no clustering” (dashed line) and “max clustering” (solid line) models for the missing baryons (see Section 3.2.1), interpolating between the \tilde{e}_{env} values recorded at the location of each SPARC galaxy. The thin blue lines show the statistical 1σ uncertainty for each clustering model. The agreement of \tilde{e}_{env} with the median values of \tilde{e}_{fit} is remarkable and not expected a priori outside a MOND context.

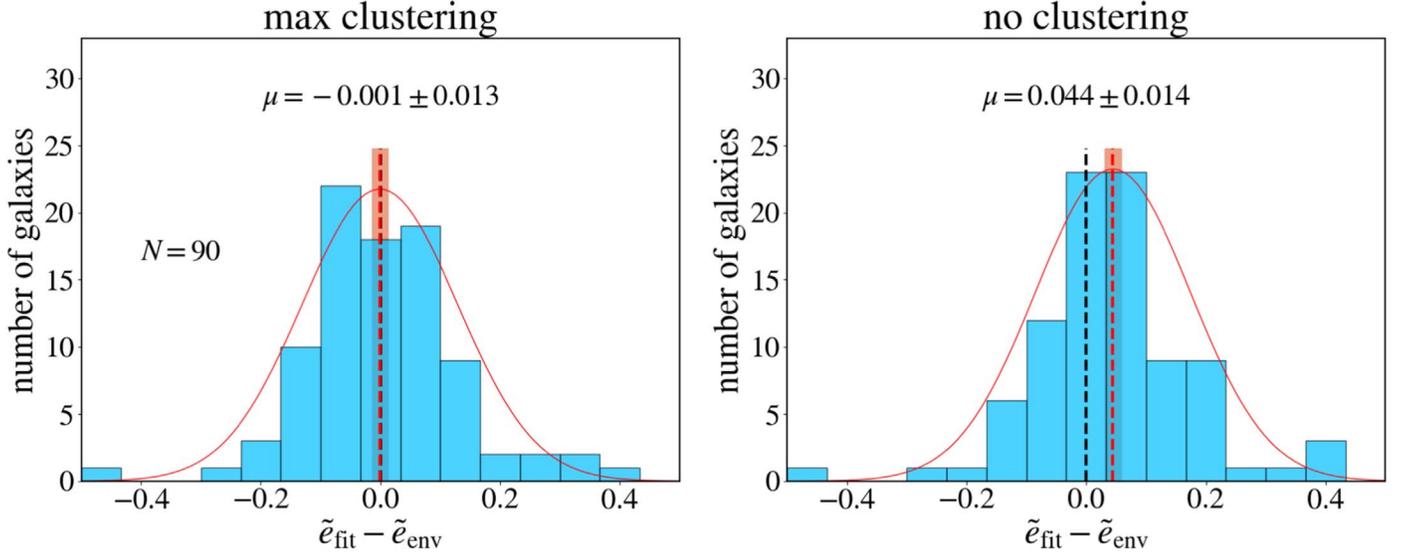


Figure 8. Statistical comparison of \tilde{e}_{fit} and \tilde{e}_{env} for the subsample of 90 SPARC galaxies shown in Figure 7. The “max clustering” and “no clustering” cases (see Section 3) are considered. The excellent statistical match with the “max clustering” model indicates that “missing” cosmic baryons are strongly correlated with observed structures.

large-scale structure extends qualitatively across the whole sky (Figure 4).

Next, we compare the RC-fitted values of \tilde{e} with fully independent estimates of the Newtonian fields from the

baryonic mass distribution in the nearby universe (using the 2M++, NSA, Karachentsev, and MCXC catalogs). We include corrections for undetected galaxies below the magnitude limits of the surveys, for cold and hot gas in galaxies, for the

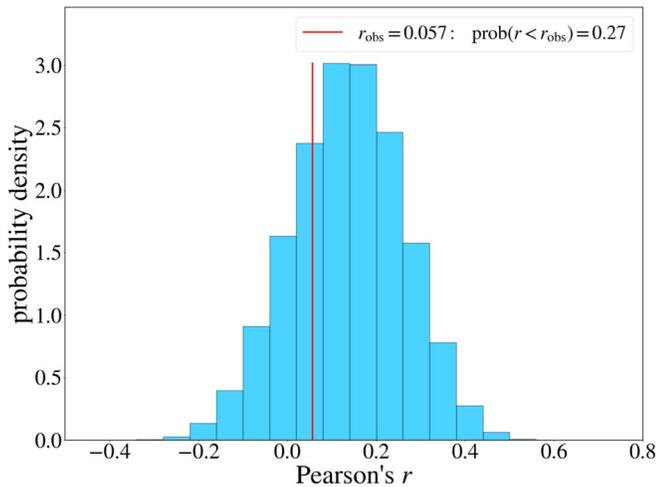


Figure 9. Observed value of Pearson’s linear correlation coefficient r between \tilde{z}_{env} and \tilde{z}_{fit} for the sample shown in Figures 7 and 8 (red line) and the expected probability distribution from many Monte Carlo realizations assuming $\tilde{z}_{\text{fit}} = \tilde{z}_{\text{env}}$ and scattering by the measured uncertainties of both quantities (histogram). For \tilde{z}_{env} we use the average of the “max clustering” and “no clustering” cases.

intracluster medium, and for the possible presence of “missing baryons” in the warm-hot intergalactic medium, with full propagation of uncertainties in a Monte Carlo framework. We find good agreement between \tilde{z}_{fit} with \tilde{z}_{env} values, in both their distance dependence (Figure 7) and the average value of the Newtonian field (Figure 8). In particular, \tilde{z}_{fit} is well matched with \tilde{z}_{env} when the missing baryons needed to bring the local baryon density into agreement with big bang nucleosynthesis ($\Omega_b h^2 = 0.022$; Cooke et al. 2018) are strongly clustered with galaxies and galaxy clusters.

The qualitative correlation between \tilde{z}_{fit} and \tilde{z}_{env} is not very sensitive to the functional form assumed for the EFE model (Equation 2) because the relative values of inferred field strengths are similar for different models. However, the absolute value of \tilde{z}_{fit} may vary, leading to systematically different mean and median values. For example, we fitted RCs using an alternative function based on numerical simulations (Haghi et al. 2019) and found a systematic shift of ~ 0.02 in \tilde{z} on average (Figure 10). Until the fitted values of \tilde{z} of Equation (2) are thoroughly tested through realistic numerical simulations of disk galaxies, systematic shifts of order ~ 0.02 are possible. This could have implications for the abundance and clustering of cosmic baryons. Our current values of \tilde{z}_{fit} are within the limits set by the “max clustering” and “no clustering” models of missing baryons, although the “max clustering” case is preferred (Figures 7 and 8).

It may be possible for $g_{\text{Ne,env}}$ to exceed the prediction of the “max clustering” model owing to the gravitating scalar fields present in some relativistic MOND theories, such as that of Skordis & Zlošnik (2021). Indeed, the EFE may manifest itself somewhat differently in this theory than in AQUAL and QUMOND because the free function in the Lagrangian (which plays the role of the IF in AQUAL) has an oscillating piece related to the time variation of the scalar field, as well as a more traditional MOND term. It will therefore be important to determine the exact behavior of the EFE in this and similar theories.

The agreement between the external fields from RC fits and large-scale structure of baryonic matter that we have discovered

is predicted by MOND modified gravity theories, supplementing the evidence for the EFE (and a fortiori a violation of the SEP) presented in Paper I. This correlation is nontrivial from the Λ CDM point of view. It is not naturally expected that the density of the cosmic web would affect the dynamics of the disk in the inner region of the DM halo, never mind in a manner mimicking the MOND EFE. We are not aware of any Λ CDM simulations predicting that RCs in stronger-field regions would tend to decline while those in low-density regions do not. This adds to the “small-scale problems” with Λ CDM (Kroupa 2012; Bullock & Boylan-Kolchin 2017). In this context, we note that challenges to Λ CDM cosmology have also been emphasized recently on the scales of galaxy clusters and voids (Haslbauer et al. 2020; Asencio et al. 2021).

The external Newtonian fields encapsulated in \tilde{z} will provide a benchmark for more detailed numerical studies of the MOND EFE, taking full account of the relative orientation of the external field and the three-dimensional morphology and kinematics of galactic disks. Various MOND theories may have different EFE predictions for RCs of disk galaxies under the same $g_{\text{Ne,env}}$. Although our fitted values of \tilde{z} are model dependent, they are empirical in nature and may distinguish existing theories when accurate numerical results become available. Here we used a fitting function that approximately agrees with existing AQUAL simulations (see Appendix A), so the agreement between $g_{\text{Ne,fit}}$ and $g_{\text{Ne,env}}$ may indicate that AQUAL is close to the correct nonrelativistic theory.

Besides distinguishing between MOND formulations, our results may be used to infer the properties of “missing baryons” in a MOND context. Our preliminary result in this regard is that baryons in the warm-hot intergalactic medium needed for $\Omega_b \simeq 0.046$ (Macquart et al. 2020) are likely strongly clustered with galaxies and clusters.

In summary, the agreement between our fit results and the observed baryonic large-scale structure matches well the MOND prediction and reinforces the detection of the EFE in Paper I, pointing to a breakdown of the SEP. These results support the modified gravity hypothesis and reveal the possibility of using the internal dynamics of galaxies to study the large-scale distribution of cosmic baryons.

We thank Indranil Banik, Andrey Kravtsov, Pengfei Li, Mordehai Milgrom, Ravi Sheth, and Paolo Tozzi for useful discussions. We also thank the anonymous referee for insightful comments that helped us improve the presentation significantly. K.-H.C. is supported by the National Research Foundation of Korea (NRF) grant funded by the Korea government (MSIT) (No. NRF-2019R1F1A1062477). H.D. is supported by St John’s College, Oxford, and acknowledges financial support from ERC grant No. 693024 and the Beecroft Trust. S.S.M. is supported in part by NASA ADAP 80NSSC19k0570 and NSF PHY-1911909.

Appendix A

A Simple One-dimensional Formalism for the EFE

In the MOND context, it is hard to quantify generally the effect of a constant external gravitational field on a galaxy disk because, for a test particle along a given orbit, the angle between the internal acceleration and the external gravitational field will vary continually, leading to a time-varying EFE. Broadly speaking, we expect that the outermost orbits will become slightly noncircular and possibly tilted with respect to

the inner galaxy plane. Asymmetric, lopsided, and/or warped HI disks are frequently observed in nearby galaxies (e.g., Sancisi et al. 2008), but their relation to the EFE can only be studied with detailed numerical simulations. For example, Brada & Milgrom (2000) show that the asymmetric warp of the Milky Way may be induced by the EFE from the Magellanic Clouds, while Banik et al. (2020) reproduce the dynamical properties of the Local Group spiral galaxy M33 as the result of the EFE from Andromeda. The main EFE, however, is a decrease in the circular velocity in the MOND regime.

In this work we are particularly interested in how the EFE depends on the external Newtonian field. Here we describe a simple one-dimensional formalism to model the EFE-induced outer decline of RCs, neglecting higher-order effects due to the full three-dimensional nature of the problem, such as the development of noncircular motions, warps, and asymmetries. Incidentally, this formalism turns out to be equivalent in AQUAL and QUMOND with a heuristic MOND relation for the constant external field.

A.1. The EFE in AQUAL and QUMOND

If a system is freely falling under a constant MOND external field g_e and we approximate the EFE by a one-dimensional AQUAL equation (see Section 6.3 of Famaey & McGaugh 2012), the gravitational acceleration g of a test particle within the system can be determined by

$$\mu\left(\frac{g + g_e}{a_0}\right)g + \left[\mu\left(\frac{g + g_e}{a_0}\right) - \mu\left(\frac{g_e}{a_0}\right)\right]g_e = g_N, \quad (\text{A1})$$

where g_N is the internal Newtonian field and $\mu(x)$ is the MOND IF. If we assume the simple IF $\mu(x) = x/(1+x)$, then the ratio g/g_N is given by Equation (6) of Paper I as

$$\nu_e(y) = \frac{1}{2} + \sqrt{\left(\frac{1}{2} - e\frac{A_e}{y}\right)^2 + \frac{B_e}{y} - e\frac{A_e}{y}}, \quad (\text{A2})$$

where $A_e = (1 + e/2)/(1 + e)$, which is redefined here so that its limit tends to 1, and $B_e = 1 + e$. For typical values $e \lesssim 0.1$ (Paper I) we have $A_e \approx B_e \approx 1$. It is then apparent that the EFE-dominating last term scales approximately linearly with e . For $e \rightarrow 0$ (i.e., truly isolated galaxies), one recovers $\nu_0(y) = 1/2 + \sqrt{1/4 + 1/y}$, which is the inverse function of the simple IF.

If the external Newtonian field of the above system is g_{Ne} and we use the QUMOND formalism, g is given by

$$g = \nu\left(\frac{g_N + g_{Ne}}{a_0}\right)g_N + \left[\nu\left(\frac{g_N + g_{Ne}}{a_0}\right) - \nu\left(\frac{g_{Ne}}{a_0}\right)\right]g_{Ne}, \quad (\text{A3})$$

where $\nu(y) = \nu_0(y)$. Then, the ratio g/g_N is given by Equation (2). Although it is not obvious algebraically, one can show that Equation (2) is equivalent to Equation (A2) for positive (physical) external field with the transformation $e^2/(1+e) = e_N$. This means that although Equation (2) is derived directly from Equation (A3), it is also consistent with Equation (A1).

A.2. Comparison with the Analytic Point-mass Weak-field Limit and Numerical Simulations

Our fitting function (Equation (2)) is a heuristic first-order model of EFE that happens to be equivalent in AQUAL and QUMOND with the correspondence $\tilde{e} = e/\sqrt{1+e}$. For general dynamical systems, for the same Newtonian external field, these two Lagrangian theories predict different values of the ratio g/g_N , which can be calculated only through numerical methods. Here we compare Equation (2) with analytic solutions of a point mass in the deep-MOND limit, as well as previously published numerical results.

Far away from any finite mass distribution, the point-mass approximation will be valid regardless of the mass distribution. For the QUMOND EFE limit, we start from Equation (60) of Milgrom (2010), which gives the approximate analytic internal potential ψ for a point mass M under an external Newtonian field of strength $g_{Ne} = e_N a_0$. Taking the gradient of ψ and considering an angle θ between g_{Ne} and the rotation axis of a test particle on a quasi-circular orbit, the azimuthal average of the radial acceleration $g = |\hat{r} \cdot \vec{\nabla}\psi|$ is given by

$$\langle g \rangle_{\text{QUMOND}} = \frac{GM}{r^2} \nu_0(y) \left(1 + \frac{\hat{\nu}_0(y)}{2}\right) \left(1 - \frac{\hat{\nu}_0(y)}{2 + \hat{\nu}_0(y)} \frac{\sin^2 \theta}{2}\right) \Bigg|_{y=e_N}, \quad (\text{A4})$$

where $\nu_0(y) = 1/2 + \sqrt{1/4 + 1/y}$ and $\hat{\nu}_0(y) \equiv d \ln \nu_0(y) / d \ln y$, which tends to $-1/2$ at large r . Thus, at large r the two extreme cases $\theta = 0^\circ$ and $\theta = 90^\circ$ show a difference of just 1/6 of the value. In other words, the direction of the external field has a minor effect. Similarly, for the AQUAL limit, we start from Equation (66) of Milgrom (2010) considering the MOND external field $g_e = e a_0$ and obtain

$$\langle g \rangle_{\text{AQUAL}} = \frac{GM}{r^2} \frac{1}{\mu_0(x) \sqrt{1 + L_0(x)}} \left(1 - \frac{L_0(x)}{1 + L_0(x)} \frac{\sin^2 \theta}{2}\right)^{-1/2} \Bigg|_{x=e}, \quad (\text{A5})$$

where $\mu_0(x) = x/(1+x)$ and $L_0(x) \equiv d \ln \mu_0(x) / d \ln x$.

As for numerical results on the ratio g/g_N , we consider a functional relation derived by Haghi et al. (2019) from AQUAL-based numerical simulations of fully pressure-supported spherical systems. In a spherical shell of radius r of a pressure-supported system, the measured velocity dispersion is a collective representation of various random orbits at different angles with respect to the external field. In this sense the velocity dispersion may capture a direction-averaged EFE. Then, for the case of an isotropic velocity distribution, the radial acceleration is given by $g(r) = 3\sigma^2/r$, where σ is the one-dimensional velocity dispersion. Thus, comparing σ with and without an external field, one can obtain an EFE-dependent $g(r)/g_N(r)$. Haghi et al. (2019) used the so-called ‘‘standard’’ IF (e.g., Famaey & McGaugh 2012) for their simulations, so we transform their result to that for the simple IF by multiplying the EFE-dependent $g(r)/g_N(r)$ by the ratio of the simple IF to the standard IF.

In Figure 10 we compare our EFE model (Equation (A2), or equivalently Equation (2)) with the numerical result by Haghi et al. (2019) and the weak-field analytic expectations of QUMOND (Equation (A4)) and AQUAL (Equation (A5)). We note that QUMOND predicts 7% higher g in the deep-MOND limit. At $\log(g_N/m \text{ s}^{-2}) \approx -10.8$ our model matches the numerical result, but at higher (lower) accelerations our g is

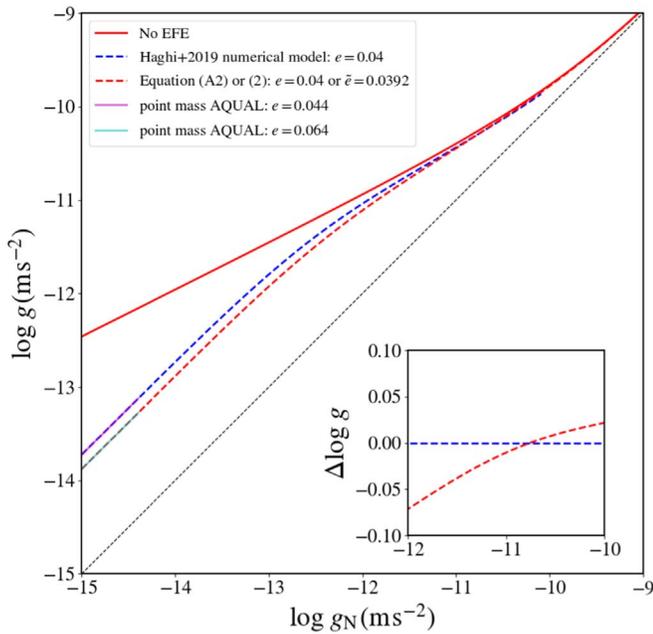


Figure 10. The one-dimensional EFE model from Equation (A2) (red dashed curve), or equivalently Equation (2) with $\tilde{e} = e/\sqrt{1+e}$, is compared with the numerical simulation result by Haghi et al. (2019) (blue dashed curve). These are then compared with the analytic point-mass weak-field limit for different values of e , considering an average angle of 60° between the external field and the axis of a circular orbit. In the acceleration range probed by the SPARC RCs, the difference between our model and the numerical result is relatively small in terms of e (or \tilde{e}). See the text for further details.

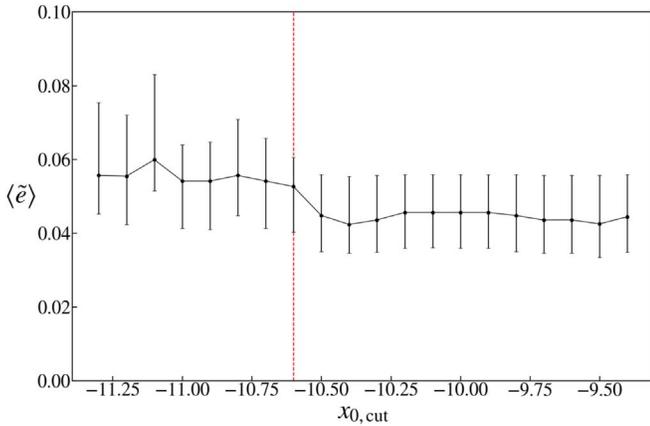


Figure 11. Dependence of the sample median of \tilde{e} on the sample selection cut. Each sample is selected by $x_{0,3} < x_{0,\text{cut}}$, where $x_{0,3}$ is the third-lowest value of x_0 as defined in Paper I (see the text for the details). The vertical dashed line indicates our selection. The error bars indicate bootstrap uncertainties. As $x_{0,\text{cut}}$ increases, galaxies without enough low-acceleration RC points start to be included in the sample so that $\langle \tilde{e} \rangle$ is biased to a lower value.

higher (lower) than the numerical value. This means that for a declining RC covering the low acceleration range $\log(g_N/\text{m s}^{-2}) < -10.8$ our model will give a lower value of \tilde{e} than the numerical model. For $\log(g_N/\text{m s}^{-2}) > -10.8$ the opposite may occur occasionally. In the weak-field limit, both our model and the numerical result give lower g than the point-mass expectation. Our model function with $e = 0.040$ matches the AQUAL point-mass limit with $e = 0.064$, exhibiting a difference of 0.024, whereas the numerical result exhibits a smaller difference of 0.004. Thus, the difference between our model and the numerical result for $\log(g_N/\text{m s}^{-2}) < -10.8$ is

0.020 in terms of the AQUAL point-mass limit. A similar median difference of ~ 0.02 in the fitted value of \tilde{e} is found from fitting the observed RCs. This is smaller than the typical individual uncertainties of ~ 0.04 – 0.05 in \tilde{e} .

Appendix B Fitted Values of the Parameters and the Newtonian Environmental Fields

Here we provide the fitted values of \tilde{e} and galactic parameters for all 162 galaxies considered in this work. We also describe how we select a statistical sample of 143 galaxies whose RCs reach low enough accelerations for the fitted \tilde{e} values to be meaningful. As illustrated in Figure 4 of Paper I, only RCs that reach low enough accelerations can probe the EFE from the large-scale distribution of cosmic mass. In other words, if we used only RCs in a high acceleration range, then the g_N – g relation would have little sensitivity to \tilde{e} (or e), and consequently the median of fitted \tilde{e} (or e) for such RCs will be biased toward zero. We therefore select the RCs that can probe a low-acceleration regime. We use the parameter x_0 introduced in Paper I, which is obtained by projecting a point $(\log g_{\text{bar}}, \log g_{\text{obs}})$ (here g_{bar} means g_N) to the curve corresponding to a flat RC (the red solid curve in Figure 10). An RC having low enough values of x_0 is expected to have sensitivity to \tilde{e} (or e), so we require an RC to have at least 3 data points $(\log g_{\text{bar}}, \log g_{\text{obs}})$ satisfying $x_0 < x_{0,\text{cut}}$. Here we do this by $x_{0,3} < x_{0,\text{cut}}$, where $x_{0,3}$ is the third-lowest value of x_0 . For the threshold we choose $x_{0,\text{cut}} = -10.6$, so that selected RCs have at least three values of 10^{x_0} lower than $10^{-10.6} \text{ m s}^{-2}$. Figure 11 shows that, at a higher threshold than this value, the median of \tilde{e} starts to decrease, indicating that the selected sample starts to be affected by about 20 RCs in a high acceleration range with little sensitivity to \tilde{e} .

Because x_0 is always on a flat RC by construction, when we select RCs by x_0 , there is no selection bias to a more declining (or rising) RC. This can be seen clearly in Figure 11: as the threshold $x_{0,\text{cut}}$ decreases from -10.6 , the sample median of \tilde{e} remains the same. However, if one selects RCs by requiring $\log g_{\text{obs}}(R)$ to be lower than a certain threshold, then the selection is biased in favor of more declining RCs. This is because for a given $g_{\text{bar}}(R)$ lower values of $g_{\text{obs}}(R)$, and thus declining RCs, are more likely to be selected by chance owing to the unavoidable observational scatter in $g_{\text{obs}}(R)$. Selection based on $\log g_{\text{bar}}(R)$ is biased in the opposite sense. Namely, less declining RCs are more likely to be selected by requiring a certain number of values of x to be lower than a certain threshold. This is because for a given $g_{\text{obs}}(R)$ a more declining Newtonian RC $g_{\text{bar}}(R)$ is more likely to be selected by chance. Our selection based on x_0 is robust against possible bias.

Figure 12 shows the distribution of the fitted \tilde{e} values for the selected sample of 143 galaxies, as well as for the full sample. The median values for the samples are $\langle \tilde{e} \rangle = 0.044^{+0.012}_{-0.009}$ (full sample) and $\langle \tilde{e} \rangle = 0.053^{+0.008}_{-0.012}$ (selected sample), the latter of which corresponds to $\langle g_{\text{Ne}} \rangle \simeq 0.0028 a_0$. Here the uncertainty is estimated from the Monte Carlo distribution of the medians of many bootstrap resamples of the data (this method is simply referred to as “bootstrap” in this paper). This is a $\sim 4.4\sigma$ detection of positive \tilde{e} . Also, from the histogram we have 97 cases of $\tilde{e} > 0$ out of 143. The null hypothesis that \tilde{e} is as likely to be < 0 as > 0 is ruled out at 4.1σ confidence based on binomial statistics. For the (contaminated) full sample the significance of $\tilde{e} > 0$ is 3.5σ by binomial statistics. These

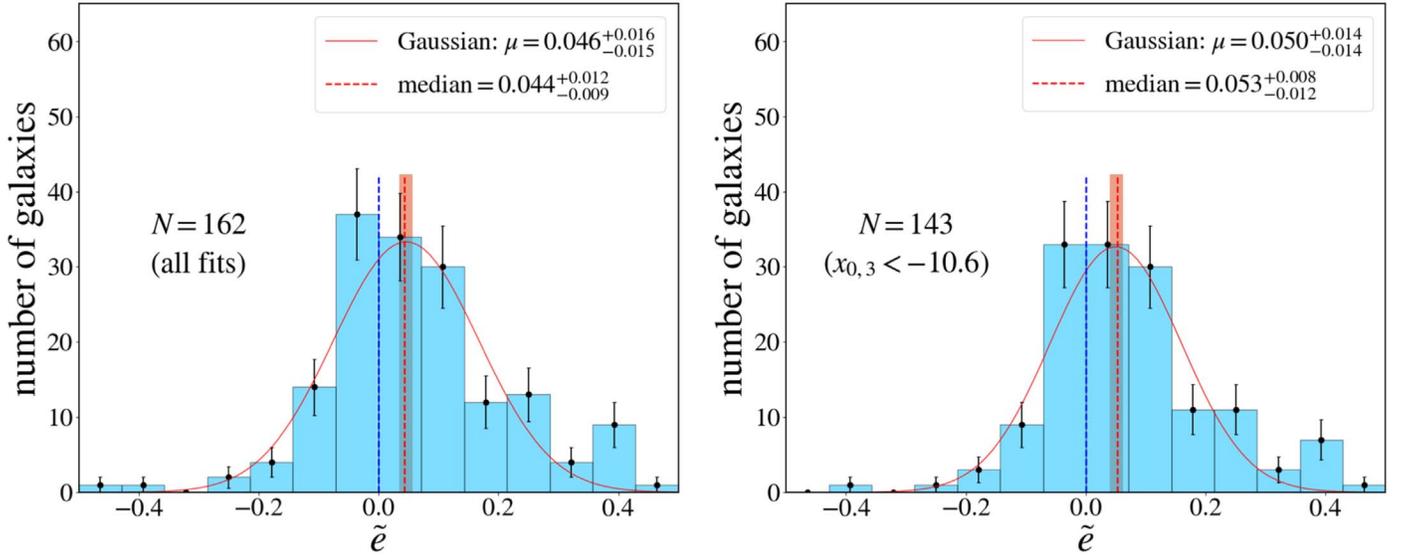


Figure 12. Distribution of the fitted values of $\tilde{\epsilon}$. The left panel shows 162 SPARC galaxies with reliable RCs ($Q < 3$; see Lelli et al. 2016), while the right panel shows our selected sample of 143 galaxies with RCs sensitive to the EFE, as indicated in Figure 11. The error bars on the histogram show Poissonian uncertainties $\sqrt{N_j}$, where N_j is the number of galaxies in each bin. The red curve indicates a Gaussian fit whose rms width is ~ 0.11 . The uncertainty on the median or on the Gaussian mean is estimated through a bootstrap method.

results reinforce the results by Paper I based on Equation (A2) and a different sample selection.

Table 2 lists the RC-fitted values of the model parameters for all 162 SPARC galaxies modeled through MCMC simulations. Values of $x_{0,3}$ (the third-lowest value of x_0 as defined above) are given for the purpose of selecting galaxies with $x_{0,3} < -10.6$ for statistical analyses. The fitted value and its uncertainty are derived from the 50th percentile and the 15.9th and 84.1th percentiles of the posterior pdf, respectively.

We assign four quality flags based on the shape of the $\tilde{\epsilon}$ posterior: P, A, B, C. In most cases the pdf is well peaked and the 50th percentile agrees well with the best fit. Those galaxies are assigned pdf quality “P.” An example (NGC 5055) is exhibited in Figure 13 (top left panel). For the remaining 24 galaxies with quality flags A, B, or C, the pdf of $\tilde{\epsilon}$ extends beyond the prior range $-0.5 < \tilde{\epsilon} < +0.5$ and is not well peaked in some cases. For nine galaxies with pdf quality “A,” the pdf is well peaked within or a little outside the prior limits.

An example (F563-V2) for this type is exhibited in Figure 13 (top right panel). For eight galaxies with pdf quality “B” the pdf has a peak with a long tail in the positive direction of $\tilde{\epsilon}$. An example (NGC 2976) for this type is exhibited in Figure 13 (bottom left panel). Finally, for seven galaxies with pdf quality “C,” the pdf is not well peaked but stays nearly flat as $\tilde{\epsilon}$ increases. An example (F579-V1) for this type is exhibited in Figure 13 (bottom right panel). For the galaxies with pdf quality of “A,” “B,” or “C,” the lower bound is still within the prior range. For those galaxies, the given value of $\tilde{\epsilon}$ in Table 2 may be considered as a lower bound within the prior range.

Table 3 lists the Newtonian environmental field strengths of 109 SPARC galaxies residing in the SDSS footprint for the “max clustering” and “no clustering” cases as described in Section 3.2.

Tables are also provided at <http://home.sejong.ac.kr/~chae> and <http://astroweb.cwru.edu/SPARC/>.

Table 2
Fitted Model Parameters

Galaxy	pdf Quality	$x_{0.3}$	\bar{z}	D (Mpc)	i (deg)	Υ_{gas}	Υ_{disk}	Υ_{bulge}
CamB	C	-11.629	$0.459^{+0.030}_{-0.055}$	$3.12^{+0.22}_{-0.21}$	$60.74^{+4.80}_{-4.67}$	$1.28^{+0.12}_{-0.11}$	$0.34^{+0.06}_{-0.05}$...
D512-2	P	-11.421	$0.106^{+0.117}_{-0.081}$	$15.94^{+4.82}_{-3.73}$	$61.25^{+9.10}_{-9.10}$	$1.36^{+0.13}_{-0.12}$	$0.52^{+0.13}_{-0.11}$...
D564-8	P	-11.987	$0.064^{+0.026}_{-0.025}$	$8.75^{+0.28}_{-0.27}$	$61.38^{+7.48}_{-7.61}$	$1.37^{+0.13}_{-0.12}$	$0.41^{+0.10}_{-0.08}$...
D631-7	P	-11.656	$-0.089^{+0.017}_{-0.019}$	$7.48^{+0.17}_{-0.17}$	$38.72^{+2.36}_{-2.27}$	$1.12^{+0.10}_{-0.09}$	$0.26^{+0.05}_{-0.04}$...
DDO 064	P	-11.113	$0.053^{+0.110}_{-0.079}$	$6.83^{+2.12}_{-1.50}$	$63.19^{+4.68}_{-4.67}$	$1.35^{+0.13}_{-0.12}$	$0.53^{+0.13}_{-0.10}$...
DDO 154	P	-11.686	$0.008^{+0.008}_{-0.008}$	$3.86^{+0.17}_{-0.16}$	$61.88^{+2.64}_{-2.55}$	$1.42^{+0.11}_{-0.11}$	$0.20^{+0.03}_{-0.03}$...
DDO 161	P	-11.549	$-0.045^{+0.010}_{-0.010}$	$3.36^{+0.40}_{-0.30}$	$73.87^{+8.01}_{-7.98}$	$1.37^{+0.13}_{-0.12}$	$0.33^{+0.07}_{-0.06}$...
DDO 168	P	-11.057	$-0.212^{+0.053}_{-0.065}$	$4.05^{+0.20}_{-0.19}$	$35.60^{+3.72}_{-3.58}$	$1.24^{+0.12}_{-0.11}$	$0.44^{+0.11}_{-0.09}$...
DDO 170	P	-11.545	$0.037^{+0.020}_{-0.017}$	$11.81^{+1.86}_{-1.50}$	$66.27^{+6.65}_{-6.42}$	$1.28^{+0.12}_{-0.11}$	$0.67^{+0.14}_{-0.12}$...
ESO 079-G014	P	-10.556	$-0.031^{+0.057}_{-0.058}$	$28.02^{+4.54}_{-3.88}$	$79.98^{+4.55}_{-4.63}$	$1.38^{+0.13}_{-0.12}$	$0.56^{+0.11}_{-0.09}$...
ESO 116-G012	P	-10.999	$-0.066^{+0.043}_{-0.044}$	$13.40^{+2.45}_{-2.01}$	$74.69^{+2.91}_{-2.92}$	$1.39^{+0.13}_{-0.12}$	$0.46^{+0.10}_{-0.08}$...
ESO 444-G084	P	-11.107	$-0.095^{+0.030}_{-0.035}$	$4.68^{+0.45}_{-0.41}$	$33.05^{+3.02}_{-2.90}$	$1.34^{+0.13}_{-0.12}$	$0.47^{+0.12}_{-0.09}$...
ESO 563-G021	P	-10.569	$-0.032^{+0.033}_{-0.035}$	$66.25^{+8.04}_{-7.19}$	$83.63^{+2.77}_{-2.82}$	$1.45^{+0.14}_{-0.13}$	$0.69^{+0.10}_{-0.09}$...
F563-1	P	-11.698	$0.112^{+0.066}_{-0.052}$	$53.07^{+10.20}_{-8.42}$	$37.60^{+4.00}_{-3.86}$	$1.35^{+0.13}_{-0.12}$	$0.61^{+0.12}_{-0.10}$...
F563-V2	A	-11.145	$0.179^{+0.152}_{-0.124}$	$63.34^{+11.89}_{-10.21}$	$49.74^{+7.26}_{-7.16}$	$1.34^{+0.13}_{-0.12}$	$0.64^{+0.15}_{-0.12}$...
F565-V2	P	-11.433	$-0.016^{+0.047}_{-0.050}$	$51.95^{+10.61}_{-8.86}$	$65.71^{+8.93}_{-9.00}$	$1.36^{+0.13}_{-0.12}$	$0.50^{+0.13}_{-0.10}$...
F568-1	P	-11.014	$-0.033^{+0.100}_{-0.100}$	$89.63^{+9.69}_{-8.74}$	$32.63^{+4.65}_{-4.54}$	$1.34^{+0.13}_{-0.12}$	$0.59^{+0.15}_{-0.12}$...
F568-3	P	-11.365	$0.238^{+0.104}_{-0.081}$	$84.40^{+8.27}_{-7.59}$	$62.04^{+7.10}_{-6.94}$	$1.42^{+0.13}_{-0.12}$	$0.47^{+0.08}_{-0.08}$...
F568-V1	P	-11.227	$0.098^{+0.096}_{-0.055}$	$85.42^{+8.23}_{-7.47}$	$64.08^{+6.73}_{-6.36}$	$1.32^{+0.12}_{-0.11}$	$0.81^{+0.16}_{-0.13}$...
F571-8	A	-11.087	$-0.423^{+0.052}_{-0.047}$	$28.31^{+3.66}_{-2.73}$	$82.96^{+4.27}_{-5.09}$	$1.38^{+0.13}_{-0.12}$	$0.23^{+0.04}_{-0.04}$...
F571-V1	P	-11.480	$0.206^{+0.134}_{-0.108}$	$80.24^{+7.94}_{-7.25}$	$44.18^{+8.08}_{-8.24}$	$1.38^{+0.13}_{-0.12}$	$0.47^{+0.11}_{-0.09}$...
F574-1	P	-11.170	$0.079^{+0.048}_{-0.042}$	$100.40^{+9.48}_{-8.66}$	$75.12^{+7.08}_{-7.12}$	$1.32^{+0.12}_{-0.11}$	$0.78^{+0.14}_{-0.12}$...
F579-V1	C	-11.130	$0.425^{+0.054}_{-0.089}$	$87.49^{+8.38}_{-7.64}$	$44.32^{+5.05}_{-4.59}$	$1.32^{+0.12}_{-0.11}$	$0.58^{+0.11}_{-0.09}$...
F583-1	P	-11.392	$0.032^{+0.055}_{-0.051}$	$35.78^{+8.42}_{-6.84}$	$67.60^{+4.53}_{-4.46}$	$1.24^{+0.11}_{-0.10}$	$0.96^{+0.16}_{-0.15}$...
F583-4	P	-11.393	$0.081^{+0.079}_{-0.062}$	$52.51^{+10.61}_{-8.74}$	$64.47^{+8.40}_{-8.26}$	$1.37^{+0.13}_{-0.12}$	$0.49^{+0.12}_{-0.10}$...
IC 2574	P	-11.599	$0.072^{+0.016}_{-0.014}$	$4.01^{+0.19}_{-0.18}$	$81.40^{+4.56}_{-4.83}$	$1.66^{+0.13}_{-0.12}$	$0.19^{+0.03}_{-0.02}$...
IC 4202	P	-10.370	$0.169^{+0.053}_{-0.048}$	$99.01^{+7.73}_{-7.19}$	$89.33^{+0.47}_{-0.74}$	$1.26^{+0.11}_{-0.11}$	$0.90^{+0.09}_{-0.09}$	$0.44^{+0.04}_{-0.04}$
KK 98-251	P	-11.418	$0.269^{+0.125}_{-0.099}$	$7.38^{+1.68}_{-1.52}$	$62.87^{+4.56}_{-4.52}$	$1.37^{+0.13}_{-0.12}$	$0.47^{+0.12}_{-0.09}$...
NGC 0024	P	-10.977	$-0.004^{+0.017}_{-0.016}$	$7.47^{+0.35}_{-0.34}$	$67.25^{+2.71}_{-2.70}$	$1.34^{+0.13}_{-0.12}$	$0.99^{+0.11}_{-0.10}$...
NGC 0055	P	-11.385	$0.050^{+0.021}_{-0.019}$	$1.94^{+0.09}_{-0.09}$	$75.20^{+3.15}_{-3.11}$	$1.33^{+0.12}_{-0.11}$	$0.21^{+0.04}_{-0.03}$...
NGC 0100	P	-11.304	$-0.106^{+0.039}_{-0.044}$	$9.64^{+1.88}_{-1.56}$	$88.80^{+0.75}_{-0.91}$	$1.39^{+0.14}_{-0.12}$	$0.39^{+0.09}_{-0.07}$...
NGC 0247	P	-11.096	$0.182^{+0.056}_{-0.046}$	$3.76^{+0.19}_{-0.18}$	$75.58^{+2.82}_{-2.82}$	$1.29^{+0.12}_{-0.11}$	$1.03^{+0.12}_{-0.11}$...
NGC 0289	P	-11.673	$0.118^{+0.031}_{-0.026}$	$19.90^{+3.16}_{-2.65}$	$54.33^{+4.10}_{-4.00}$	$1.43^{+0.13}_{-0.12}$	$0.44^{+0.07}_{-0.06}$...
NGC 0300	P	-11.496	$-0.009^{+0.026}_{-0.026}$	$2.03^{+0.10}_{-0.09}$	$47.22^{+5.34}_{-4.57}$	$1.34^{+0.13}_{-0.12}$	$0.40^{+0.08}_{-0.06}$...
NGC 0801	P	-10.840	$0.174^{+0.024}_{-0.023}$	$68.41^{+6.50}_{-5.84}$	$79.93^{+1.01}_{-1.00}$	$1.44^{+0.14}_{-0.13}$	$0.60^{+0.07}_{-0.06}$...
NGC 0891	P	-10.407	$-0.118^{+0.022}_{-0.022}$	$9.83^{+0.46}_{-0.44}$	$89.32^{+0.48}_{-0.73}$	$1.34^{+0.13}_{-0.11}$	$0.33^{+0.02}_{-0.02}$	$0.52^{+0.06}_{-0.06}$
NGC 1003	P	-11.640	$-0.056^{+0.008}_{-0.009}$	$6.53^{+0.65}_{-0.58}$	$70.19^{+4.53}_{-4.49}$	$1.22^{+0.11}_{-0.10}$	$0.77^{+0.11}_{-0.10}$...
NGC 1090	P	-11.006	$0.059^{+0.024}_{-0.023}$	$31.86^{+4.65}_{-4.02}$	$65.31^{+2.89}_{-2.87}$	$1.36^{+0.13}_{-0.12}$	$0.52^{+0.09}_{-0.08}$...
NGC 2403	P	-11.512	$-0.019^{+0.005}_{-0.005}$	$3.59^{+0.13}_{-0.13}$	$72.06^{+2.27}_{-2.22}$	$0.76^{+0.06}_{-0.05}$	$0.39^{+0.02}_{-0.02}$...
NGC 2683	P	-11.126	$0.086^{+0.028}_{-0.025}$	$9.88^{+0.47}_{-0.45}$	$81.02^{+4.38}_{-4.53}$	$1.41^{+0.14}_{-0.12}$	$0.56^{+0.05}_{-0.05}$	$0.69^{+0.17}_{-0.14}$
NGC 2841	P	-11.008	$-0.028^{+0.013}_{-0.013}$	$14.02^{+0.98}_{-0.91}$	$82.96^{+4.46}_{-5.40}$	$1.31^{+0.12}_{-0.11}$	$0.91^{+0.10}_{-0.09}$	$0.96^{+0.08}_{-0.07}$
NGC 2903	P	-11.325	$0.040^{+0.008}_{-0.008}$	$12.46^{+0.97}_{-0.88}$	$69.16^{+2.76}_{-2.76}$	$1.26^{+0.11}_{-0.10}$	$0.18^{+0.02}_{-0.02}$...
NGC 2915	P	-11.655	$-0.053^{+0.013}_{-0.014}$	$4.12^{+0.20}_{-0.19}$	$62.27^{+3.41}_{-3.37}$	$1.35^{+0.13}_{-0.12}$	$0.58^{+0.11}_{-0.09}$...
NGC 2955	P	-10.505	$0.030^{+0.051}_{-0.050}$	$90.28^{+8.10}_{-7.34}$	$59.69^{+5.30}_{-4.86}$	$1.43^{+0.14}_{-0.13}$	$0.32^{+0.05}_{-0.04}$	$0.72^{+0.09}_{-0.08}$
NGC 2976	B	-10.253	$0.380^{+0.083}_{-0.112}$	$3.62^{+0.18}_{-0.17}$	$76.57^{+6.22}_{-6.12}$	$1.44^{+0.13}_{-0.12}$	$0.46^{+0.06}_{-0.06}$...
NGC 2998	P	-10.813	$0.103^{+0.029}_{-0.027}$	$69.88^{+8.60}_{-7.57}$	$58.67^{+1.94}_{-1.95}$	$1.44^{+0.14}_{-0.13}$	$0.54^{+0.09}_{-0.07}$...
NGC 3109	P	-11.535	$0.012^{+0.010}_{-0.010}$	$1.40^{+0.07}_{-0.06}$	$76.85^{+3.90}_{-3.81}$	$1.68^{+0.14}_{-0.13}$	$0.24^{+0.05}_{-0.04}$...
NGC 3198	P	-11.532	$0.055^{+0.012}_{-0.011}$	$15.27^{+1.17}_{-1.08}$	$75.62^{+2.73}_{-2.71}$	$1.36^{+0.13}_{-0.12}$	$0.43^{+0.04}_{-0.04}$...
NGC 3521	P	-10.304	$-0.116^{+0.061}_{-0.067}$	$6.59^{+1.11}_{-0.96}$	$78.29^{+4.35}_{-4.36}$	$1.42^{+0.14}_{-0.12}$	$0.57^{+0.11}_{-0.09}$...
NGC 3726	P	-11.048	$-0.002^{+0.031}_{-0.031}$	$14.33^{+1.54}_{-1.39}$	$52.19^{+1.97}_{-1.95}$	$1.34^{+0.13}_{-0.12}$	$0.44^{+0.07}_{-0.06}$...
NGC 3741	P	-11.943	$-0.016^{+0.009}_{-0.009}$	$3.10^{+0.16}_{-0.15}$	$69.51^{+3.92}_{-3.86}$	$1.35^{+0.13}_{-0.12}$	$0.34^{+0.07}_{-0.06}$...
NGC 3769	P	-11.675	$0.021^{+0.019}_{-0.018}$	$17.35^{+1.75}_{-1.59}$	$70.20^{+1.98}_{-1.97}$	$1.41^{+0.14}_{-0.12}$	$0.38^{+0.07}_{-0.06}$...
NGC 3877	A	-10.200	$0.238^{+0.157}_{-0.155}$	$17.45^{+2.06}_{-1.85}$	$76.04^{+0.99}_{-1.00}$	$1.39^{+0.13}_{-0.12}$	$0.50^{+0.08}_{-0.07}$...
NGC 3893	P	-10.658	$-0.032^{+0.048}_{-0.049}$	$18.28^{+2.06}_{-1.86}$	$49.70^{+1.91}_{-1.90}$	$1.41^{+0.14}_{-0.12}$	$0.45^{+0.07}_{-0.06}$...
NGC 3917	P	-10.822	$0.111^{+0.057}_{-0.050}$	$19.37^{+2.30}_{-2.05}$	$79.33^{+1.97}_{-1.96}$	$1.39^{+0.13}_{-0.12}$	$0.61^{+0.10}_{-0.08}$...
NGC 3949	P	-10.017	$-0.024^{+0.216}_{-0.180}$	$16.90^{+2.09}_{-1.85}$	$54.98^{+1.98}_{-1.97}$	$1.40^{+0.13}_{-0.12}$	$0.43^{+0.07}_{-0.06}$...
NGC 3953	B	-10.070	$0.390^{+0.077}_{-0.115}$	$18.83^{+2.20}_{-1.97}$	$62.12^{+1.00}_{-0.99}$	$1.41^{+0.14}_{-0.12}$	$0.60^{+0.08}_{-0.07}$...
NGC 3972	P	-10.550	$-0.096^{+0.075}_{-0.071}$	$17.03^{+2.17}_{-1.92}$	$77.01^{+1.00}_{-1.00}$	$1.38^{+0.13}_{-0.12}$	$0.46^{+0.09}_{-0.08}$...

Table 2
(Continued)

Galaxy	pdf Quality	$x_{0.3}$	\bar{z}	D (Mpc)	i (deg)	Υ_{gas}	Υ_{disk}	Υ_{bulge}
NGC 3992	P	-10.731	$0.095^{+0.030}_{-0.028}$	$24.45^{+2.10}_{-1.94}$	$56.74^{+1.92}_{-1.92}$	$1.42^{+0.14}_{-0.12}$	$0.68^{+0.09}_{-0.08}$...
NGC 4010	P	-10.715	$-0.057^{+0.051}_{-0.050}$	$16.26^{+2.01}_{-1.80}$	$88.80^{+0.75}_{-0.91}$	$1.41^{+0.14}_{-0.13}$	$0.36^{+0.07}_{-0.06}$...
NGC 4013	P	-11.065	$-0.047^{+0.015}_{-0.016}$	$14.38^{+1.35}_{-1.24}$	$88.80^{+0.75}_{-0.91}$	$1.38^{+0.13}_{-0.12}$	$0.48^{+0.08}_{-0.07}$	$0.82^{+0.20}_{-0.16}$
NGC 4051	B	-10.205	$0.335^{+0.114}_{-0.150}$	$17.29^{+2.08}_{-1.87}$	$49.32^{+2.82}_{-2.80}$	$1.39^{+0.13}_{-0.12}$	$0.48^{+0.08}_{-0.07}$...
NGC 4068	A	-11.195	$0.321^{+0.108}_{-0.109}$	$4.37^{+0.22}_{-0.21}$	$48.19^{+4.79}_{-4.97}$	$1.39^{+0.13}_{-0.12}$	$0.43^{+0.10}_{-0.08}$...
NGC 4085	P	-10.175	$-0.170^{+0.114}_{-0.106}$	$15.12^{+1.89}_{-1.67}$	$81.87^{+2.01}_{-2.02}$	$1.39^{+0.13}_{-0.12}$	$0.33^{+0.06}_{-0.05}$...
NGC 4088	P	-10.621	$0.041^{+0.049}_{-0.047}$	$14.82^{+1.68}_{-1.50}$	$68.71^{+1.99}_{-2.00}$	$1.40^{+0.13}_{-0.12}$	$0.35^{+0.05}_{-0.05}$...
NGC 4100	P	-10.925	$0.087^{+0.026}_{-0.025}$	$19.53^{+2.13}_{-1.92}$	$73.69^{+1.95}_{-1.94}$	$1.40^{+0.14}_{-0.12}$	$0.57^{+0.08}_{-0.07}$...
NGC 4138	P	-10.717	$0.111^{+0.087}_{-0.073}$	$18.72^{+2.11}_{-1.90}$	$54.34^{+2.78}_{-2.77}$	$1.40^{+0.13}_{-0.12}$	$0.56^{+0.11}_{-0.09}$	$0.68^{+0.17}_{-0.14}$
NGC 4157	P	-10.880	$-0.017^{+0.031}_{-0.031}$	$15.20^{+1.61}_{-1.46}$	$81.93^{+2.98}_{-3.02}$	$1.39^{+0.13}_{-0.11}$	$0.42^{+0.06}_{-0.06}$	$0.65^{+0.16}_{-0.13}$
NGC 4183	P	-11.314	$0.108^{+0.034}_{-0.030}$	$18.19^{+2.03}_{-1.80}$	$82.23^{+1.96}_{-1.97}$	$1.33^{+0.13}_{-0.11}$	$0.69^{+0.11}_{-0.09}$...
NGC 4214	P	-11.329	$-0.036^{+0.034}_{-0.036}$	$2.82^{+0.14}_{-0.13}$	$18.24^{+1.63}_{-1.52}$	$1.35^{+0.13}_{-0.12}$	$0.43^{+0.11}_{-0.08}$...
NGC 4217	P	-10.604	$-0.148^{+0.044}_{-0.046}$	$15.46^{+1.53}_{-1.40}$	$85.96^{+1.90}_{-1.97}$	$1.41^{+0.14}_{-0.12}$	$0.86^{+0.18}_{-0.15}$	$0.23^{+0.03}_{-0.03}$
NGC 4559	P	-11.130	$0.028^{+0.038}_{-0.036}$	$7.42^{+1.25}_{-1.03}$	$67.19^{+0.99}_{-0.99}$	$1.38^{+0.13}_{-0.12}$	$0.46^{+0.09}_{-0.07}$...
NGC 5005	P	-9.819	$-0.121^{+0.243}_{-0.191}$	$16.16^{+1.23}_{-1.23}$	$68.15^{+1.98}_{-1.96}$	$1.42^{+0.14}_{-0.12}$	$0.49^{+0.08}_{-0.08}$	$0.54^{+0.08}_{-0.07}$
NGC 5033	P	-11.306	$0.098^{+0.012}_{-0.011}$	$23.48^{+1.96}_{-1.82}$	$66.26^{+0.99}_{-0.99}$	$1.45^{+0.13}_{-0.12}$	$0.43^{+0.06}_{-0.05}$	$0.28^{+0.04}_{-0.04}$
NGC 5055	P	-11.416	$0.053^{+0.004}_{-0.004}$	$9.82^{+0.29}_{-0.28}$	$59.40^{+2.38}_{-2.19}$	$1.50^{+0.14}_{-0.12}$	$0.31^{+0.02}_{-0.02}$...
NGC 5371	P	-10.367	$0.249^{+0.042}_{-0.043}$	$16.44^{+2.49}_{-2.15}$	$52.10^{+2.01}_{-1.99}$	$1.36^{+0.13}_{-0.12}$	$1.38^{+0.23}_{-0.20}$...
NGC 5585	P	-11.208	$-0.083^{+0.032}_{-0.033}$	$5.00^{+0.81}_{-0.69}$	$51.78^{+1.95}_{-1.95}$	$1.38^{+0.13}_{-0.12}$	$0.36^{+0.07}_{-0.06}$...
NGC 5907	P	-10.991	$0.090^{+0.013}_{-0.013}$	$16.08^{+0.80}_{-0.76}$	$87.51^{+1.55}_{-1.88}$	$1.31^{+0.12}_{-0.11}$	$0.65^{+0.04}_{-0.04}$...
NGC 5985	P	-10.685	$0.174^{+0.032}_{-0.030}$	$72.59^{+8.94}_{-8.01}$	$62.13^{+1.89}_{-1.90}$	$1.34^{+0.13}_{-0.11}$	$0.43^{+0.07}_{-0.06}$	$1.86^{+0.26}_{-0.23}$
NGC 6015	P	-10.872	$-0.093^{+0.024}_{-0.026}$	$8.05^{+0.86}_{-0.78}$	$60.87^{+1.95}_{-1.93}$	$1.37^{+0.13}_{-0.12}$	$1.68^{+0.21}_{-0.18}$...
NGC 6195	P	-10.479	$-0.012^{+0.036}_{-0.036}$	$110.16^{+9.46}_{-8.67}$	$59.77^{+4.43}_{-4.21}$	$1.46^{+0.14}_{-0.13}$	$0.29^{+0.05}_{-0.04}$	$0.81^{+0.09}_{-0.08}$
NGC 6503	P	-11.601	$0.008^{+0.006}_{-0.006}$	$6.79^{+0.29}_{-0.28}$	$75.79^{+1.86}_{-1.84}$	$1.37^{+0.13}_{-0.12}$	$0.41^{+0.03}_{-0.03}$...
NGC 6674	P	-10.969	$-0.016^{+0.020}_{-0.023}$	$37.38^{+6.18}_{-5.29}$	$52.20^{+5.50}_{-5.25}$	$1.37^{+0.13}_{-0.12}$	$1.08^{+0.33}_{-0.28}$	$1.39^{+0.59}_{-0.41}$
NGC 6789	A	-10.592	$-0.268^{+0.124}_{-0.127}$	$3.52^{+0.18}_{-0.17}$	$46.93^{+6.32}_{-5.60}$	$1.35^{+0.13}_{-0.12}$	$0.51^{+0.13}_{-0.10}$...
NGC 6946	P	-10.854	$0.045^{+0.025}_{-0.027}$	$4.25^{+0.55}_{-0.49}$	$41.92^{+1.82}_{-1.81}$	$1.40^{+0.13}_{-0.12}$	$0.49^{+0.07}_{-0.06}$	$0.56^{+0.07}_{-0.06}$
NGC 7331	P	-10.758	$-0.079^{+0.018}_{-0.020}$	$12.26^{+0.89}_{-0.83}$	$74.96^{+1.99}_{-1.98}$	$1.34^{+0.12}_{-0.11}$	$0.42^{+0.04}_{-0.04}$	$0.63^{+0.14}_{-0.12}$
NGC 7793	P	-10.944	$0.233^{+0.069}_{-0.057}$	$3.59^{+0.18}_{-0.17}$	$69.18^{+6.00}_{-5.78}$	$1.44^{+0.14}_{-0.13}$	$0.33^{+0.04}_{-0.03}$...
NGC 7814	P	-10.563	$-0.110^{+0.020}_{-0.020}$	$14.75^{+0.63}_{-0.61}$	$89.33^{+0.47}_{-0.73}$	$1.40^{+0.14}_{-0.12}$	$0.83^{+0.13}_{-0.12}$	$0.58^{+0.05}_{-0.05}$
UGC 00128	P	-11.681	$0.016^{+0.007}_{-0.007}$	$49.32^{+6.79}_{-5.77}$	$52.54^{+5.71}_{-4.88}$	$1.12^{+0.10}_{-0.09}$	$1.78^{+0.21}_{-0.19}$...
UGC 00191	P	-10.944	$0.096^{+0.048}_{-0.038}$	$16.10^{+3.27}_{-2.60}$	$47.98^{+4.39}_{-4.24}$	$1.28^{+0.12}_{-0.11}$	$0.79^{+0.13}_{-0.11}$...
UGC 00634	P	-11.179	$0.028^{+0.032}_{-0.029}$	$29.84^{+6.22}_{-5.01}$	$41.35^{+5.35}_{-4.85}$	$1.39^{+0.13}_{-0.12}$	$0.45^{+0.10}_{-0.08}$...
UGC 00731	P	-11.203	$-0.243^{+0.049}_{-0.056}$	$4.39^{+0.85}_{-0.71}$	$54.98^{+3.05}_{-3.04}$	$1.22^{+0.12}_{-0.11}$	$0.61^{+0.19}_{-0.14}$...
UGC 00891	P	-11.216	$-0.113^{+0.024}_{-0.028}$	$5.43^{+0.90}_{-0.77}$	$56.28^{+5.04}_{-4.91}$	$1.34^{+0.13}_{-0.12}$	$0.42^{+0.10}_{-0.08}$...
UGC 01230	C	-11.686	$0.404^{+0.069}_{-0.100}$	$49.83^{+9.02}_{-7.50}$	$38.61^{+5.00}_{-4.63}$	$1.32^{+0.12}_{-0.11}$	$0.59^{+0.12}_{-0.10}$...
UGC 01281	P	-11.411	$0.014^{+0.019}_{-0.017}$	$5.32^{+0.24}_{-0.23}$	$89.33^{+0.47}_{-0.73}$	$1.42^{+0.13}_{-0.12}$	$0.45^{+0.09}_{-0.08}$...
UGC 02023	C	-11.154	$0.344^{+0.112}_{-0.178}$	$8.88^{+2.51}_{-1.93}$	$23.95^{+5.01}_{-4.72}$	$1.36^{+0.13}_{-0.12}$	$0.45^{+0.11}_{-0.09}$...
UGC 02259	P	-11.108	$0.198^{+0.081}_{-0.060}$	$15.96^{+3.34}_{-2.65}$	$44.35^{+2.74}_{-2.72}$	$1.30^{+0.12}_{-0.11}$	$0.89^{+0.16}_{-0.13}$...
UGC 02487	P	-11.058	$0.095^{+0.011}_{-0.011}$	$73.74^{+9.10}_{-8.02}$	$46.16^{+3.58}_{-3.44}$	$1.49^{+0.15}_{-0.13}$	$0.58^{+0.12}_{-0.10}$	$0.59^{+0.10}_{-0.09}$
UGC 02885	P	-10.968	$0.009^{+0.025}_{-0.025}$	$81.59^{+6.83}_{-6.33}$	$66.66^{+3.63}_{-3.54}$	$1.44^{+0.14}_{-0.13}$	$0.44^{+0.06}_{-0.06}$	$0.92^{+0.11}_{-0.10}$
UGC 02916	P	-10.824	$0.258^{+0.074}_{-0.060}$	$58.40^{+6.44}_{-5.72}$	$58.57^{+3.95}_{-3.81}$	$1.39^{+0.13}_{-0.12}$	$1.10^{+0.15}_{-0.13}$	$0.42^{+0.05}_{-0.04}$
UGC 02953	P	-11.147	$-0.006^{+0.006}_{-0.006}$	$13.51^{+0.87}_{-0.76}$	$64.55^{+3.06}_{-3.02}$	$1.51^{+0.15}_{-0.13}$	$0.57^{+0.03}_{-0.02}$	$0.58^{+0.02}_{-0.02}$
UGC 03205	P	-10.823	$0.004^{+0.018}_{-0.019}$	$42.35^{+4.52}_{-4.07}$	$70.74^{+3.58}_{-3.55}$	$1.33^{+0.12}_{-0.11}$	$0.63^{+0.09}_{-0.08}$	$1.30^{+0.14}_{-0.13}$
UGC 03546	P	-10.772	$0.020^{+0.022}_{-0.023}$	$24.33^{+3.31}_{-2.87}$	$60.83^{+4.33}_{-4.21}$	$1.39^{+0.13}_{-0.12}$	$0.58^{+0.10}_{-0.08}$	$0.43^{+0.06}_{-0.05}$
UGC 03580	P	-11.295	$-0.046^{+0.012}_{-0.012}$	$15.17^{+1.38}_{-1.24}$	$67.11^{+3.58}_{-3.55}$	$1.51^{+0.14}_{-0.13}$	$0.47^{+0.06}_{-0.05}$	$0.15^{+0.02}_{-0.02}$
UGC 04278	P	-10.918	$-0.181^{+0.039}_{-0.047}$	$5.85^{+0.97}_{-0.89}$	$88.01^{+1.40}_{-2.17}$	$1.38^{+0.13}_{-0.12}$	$0.37^{+0.08}_{-0.07}$...
UGC 04325	B	-10.700	$0.340^{+0.105}_{-0.119}$	$14.00^{+2.46}_{-2.13}$	$44.10^{+2.74}_{-2.70}$	$1.26^{+0.12}_{-0.11}$	$1.09^{+0.20}_{-0.17}$...
UGC 04483	P	-11.307	$0.141^{+0.051}_{-0.043}$	$3.36^{+0.31}_{-0.29}$	$58.91^{+2.95}_{-2.94}$	$1.37^{+0.13}_{-0.12}$	$0.48^{+0.11}_{-0.09}$...
UGC 04499	P	-11.197	$0.109^{+0.090}_{-0.069}$	$13.25^{+3.54}_{-2.64}$	$51.37^{+2.90}_{-2.89}$	$1.38^{+0.13}_{-0.12}$	$0.49^{+0.10}_{-0.08}$...
UGC 05005	P	-11.663	$0.133^{+0.106}_{-0.078}$	$51.40^{+10.78}_{-8.80}$	$52.27^{+8.95}_{-8.81}$	$1.42^{+0.14}_{-0.13}$	$0.39^{+0.09}_{-0.07}$...
UGC 05253	P	-11.332	$0.056^{+0.008}_{-0.008}$	$20.87^{+2.22}_{-1.95}$	$52.13^{+3.07}_{-2.99}$	$1.40^{+0.13}_{-0.12}$	$0.30^{+0.04}_{-0.03}$	$0.39^{+0.03}_{-0.03}$
UGC 05414	P	-11.015	$0.071^{+0.114}_{-0.090}$	$8.84^{+2.72}_{-2.02}$	$55.45^{+2.98}_{-2.96}$	$1.40^{+0.13}_{-0.12}$	$0.42^{+0.10}_{-0.08}$...
UGC 05716	P	-11.585	$0.087^{+0.031}_{-0.026}$	$22.14^{+3.76}_{-3.07}$	$65.53^{+7.60}_{-7.04}$	$1.25^{+0.11}_{-0.10}$	$0.86^{+0.11}_{-0.09}$...
UGC 05721	P	-11.391	$0.046^{+0.032}_{-0.029}$	$10.08^{+1.59}_{-1.36}$	$67.73^{+4.26}_{-4.23}$	$1.39^{+0.14}_{-0.12}$	$0.51^{+0.11}_{-0.09}$...
UGC 05750	P	-11.405	$0.137^{+0.080}_{-0.059}$	$62.33^{+12.27}_{-10.19}$	$72.17^{+7.93}_{-7.99}$	$1.37^{+0.13}_{-0.12}$	$0.55^{+0.13}_{-0.11}$...
UGC 05764	A	-11.286	$0.360^{+0.085}_{-0.082}$	$15.34^{+2.27}_{-2.07}$	$74.71^{+6.73}_{-6.66}$	$1.11^{+0.10}_{-0.09}$	$2.67^{+0.33}_{-0.29}$...
UGC 05829	B	-11.254	$0.115^{+0.237}_{-0.157}$	$6.86^{+2.09}_{-1.70}$	$41.85^{+9.75}_{-9.62}$	$1.27^{+0.12}_{-0.11}$	$0.69^{+0.18}_{-0.17}$...

Table 2
(Continued)

Galaxy	pdf Quality	$x_{0,3}$	\bar{z}	D (Mpc)	i (deg)	Υ_{gas}	Υ_{disk}	Υ_{bulge}
UGC 05918	P	-11.569	$0.040^{+0.077}_{-0.062}$	$7.36^{+2.40}_{-1.78}$	$48.64^{+4.88}_{-4.87}$	$1.32^{+0.13}_{-0.11}$	$0.58^{+0.15}_{-0.12}$...
UGC 05986	P	-11.159	$-0.017^{+0.037}_{-0.037}$	$12.80^{+2.32}_{-1.96}$	$88.05^{+1.37}_{-1.12}$	$1.49^{+0.15}_{-0.13}$	$0.37^{+0.08}_{-0.06}$...
UGC 05999	B	-11.309	$0.093^{+0.241}_{-0.171}$	$44.25^{+8.66}_{-7.24}$	$24.99^{+8.98}_{-7.61}$	$1.37^{+0.13}_{-0.12}$	$0.48^{+0.11}_{-0.09}$...
UGC 06399	P	-11.074	$-0.004^{+0.049}_{-0.045}$	$18.50^{+2.51}_{-2.20}$	$75.22^{+1.98}_{-1.98}$	$1.37^{+0.13}_{-0.12}$	$0.54^{+0.12}_{-0.10}$...
UGC 06446	P	-11.364	$0.139^{+0.076}_{-0.059}$	$17.29^{+3.79}_{-2.98}$	$54.16^{+2.81}_{-2.77}$	$1.28^{+0.12}_{-0.11}$	$0.92^{+0.15}_{-0.13}$...
UGC 06614	P	-11.009	$-0.070^{+0.037}_{-0.040}$	$82.52^{+8.17}_{-7.45}$	$30.92^{+3.13}_{-2.83}$	$1.42^{+0.14}_{-0.13}$	$0.47^{+0.11}_{-0.09}$	$0.57^{+0.13}_{-0.11}$
UGC 06628	C	-11.250	$0.397^{+0.075}_{-0.129}$	$11.46^{+3.33}_{-2.57}$	$19.93^{+3.87}_{-3.43}$	$1.34^{+0.13}_{-0.12}$	$0.48^{+0.11}_{-0.09}$...
UGC 06667	P	-11.279	$-0.125^{+0.025}_{-0.027}$	$15.59^{+1.82}_{-1.66}$	$88.80^{+0.75}_{-0.91}$	$1.31^{+0.12}_{-0.11}$	$0.52^{+0.14}_{-0.11}$...
UGC 06786	P	-11.242	$-0.029^{+0.012}_{-0.013}$	$46.16^{+4.34}_{-4.00}$	$68.02^{+2.73}_{-2.69}$	$1.49^{+0.14}_{-0.13}$	$0.36^{+0.05}_{-0.05}$	$0.42^{+0.04}_{-0.04}$
UGC 06818	P	-11.254	$-0.002^{+0.038}_{-0.035}$	$15.66^{+2.21}_{-1.93}$	$74.64^{+3.04}_{-3.04}$	$1.42^{+0.14}_{-0.13}$	$0.31^{+0.07}_{-0.06}$...
UGC 06917	P	-10.966	$-0.001^{+0.046}_{-0.044}$	$17.93^{+2.22}_{-1.96}$	$56.49^{+1.96}_{-1.95}$	$1.36^{+0.13}_{-0.12}$	$0.55^{+0.09}_{-0.08}$...
UGC 06923	P	-10.751	$0.035^{+0.083}_{-0.071}$	$17.20^{+2.35}_{-2.05}$	$65.02^{+1.99}_{-2.00}$	$1.38^{+0.13}_{-0.12}$	$0.44^{+0.10}_{-0.08}$...
UGC 06930	P	-11.169	$0.232^{+0.120}_{-0.092}$	$18.37^{+2.41}_{-2.14}$	$38.86^{+4.06}_{-3.91}$	$1.36^{+0.13}_{-0.12}$	$0.58^{+0.11}_{-0.09}$...
UGC 06983	P	-11.198	$0.056^{+0.037}_{-0.035}$	$19.80^{+2.31}_{-2.06}$	$49.43^{+0.98}_{-0.99}$	$1.33^{+0.13}_{-0.11}$	$0.77^{+0.12}_{-0.10}$...
UGC 07089	P	-11.240	$0.094^{+0.063}_{-0.051}$	$17.02^{+2.43}_{-2.14}$	$80.15^{+2.98}_{-2.98}$	$1.40^{+0.14}_{-0.12}$	$0.40^{+0.09}_{-0.07}$...
UGC 07125	P	-11.509	$0.122^{+0.063}_{-0.045}$	$13.44^{+3.16}_{-2.28}$	$87.98^{+1.42}_{-2.21}$	$1.27^{+0.12}_{-0.11}$	$0.69^{+0.11}_{-0.09}$...
UGC 07151	P	-10.861	$0.149^{+0.059}_{-0.049}$	$6.96^{+0.34}_{-0.32}$	$88.03^{+1.38}_{-2.15}$	$1.35^{+0.13}_{-0.12}$	$0.71^{+0.09}_{-0.08}$...
UGC 07232	P	-10.628	$-0.033^{+0.099}_{-0.087}$	$2.82^{+0.17}_{-0.16}$	$59.23^{+5.01}_{-4.98}$	$1.36^{+0.13}_{-0.12}$	$0.46^{+0.11}_{-0.09}$...
UGC 07261	B	-11.157	$0.242^{+0.153}_{-0.134}$	$12.56^{+3.23}_{-2.60}$	$42.29^{+7.11}_{-6.67}$	$1.36^{+0.13}_{-0.12}$	$0.49^{+0.10}_{-0.08}$...
UGC 07323	P	-10.849	$0.131^{+0.167}_{-0.132}$	$8.32^{+2.37}_{-1.96}$	$48.51^{+2.91}_{-2.89}$	$1.41^{+0.13}_{-0.12}$	$0.43^{+0.10}_{-0.08}$...
UGC 07399	P	-11.089	$-0.026^{+0.041}_{-0.042}$	$14.22^{+2.53}_{-2.14}$	$57.54^{+2.81}_{-2.80}$	$1.38^{+0.13}_{-0.12}$	$0.61^{+0.11}_{-0.11}$...
UGC 07524	P	-11.216	$0.154^{+0.052}_{-0.045}$	$4.72^{+0.24}_{-0.22}$	$49.72^{+2.78}_{-2.78}$	$1.24^{+0.11}_{-0.10}$	$0.90^{+0.13}_{-0.12}$...
UGC 07559	P	-11.403	$0.204^{+0.073}_{-0.055}$	$4.98^{+0.25}_{-0.24}$	$61.77^{+2.95}_{-2.97}$	$1.37^{+0.13}_{-0.12}$	$0.48^{+0.12}_{-0.10}$...
UGC 07577	B	-11.735	$0.420^{+0.056}_{-0.082}$	$2.56^{+0.13}_{-0.12}$	$63.05^{+2.94}_{-2.92}$	$1.33^{+0.12}_{-0.11}$	$0.44^{+0.09}_{-0.08}$...
UGC 07603	P	-11.259	$-0.072^{+0.035}_{-0.038}$	$4.66^{+0.80}_{-0.69}$	$78.38^{+2.94}_{-2.93}$	$1.39^{+0.13}_{-0.12}$	$0.44^{+0.10}_{-0.08}$...
UGC 07608	A	-11.489	$0.185^{+0.160}_{-0.128}$	$8.47^{+2.34}_{-1.94}$	$42.61^{+7.61}_{-7.85}$	$1.36^{+0.13}_{-0.12}$	$0.51^{+0.13}_{-0.10}$...
UGC 07690	P	-10.968	$0.224^{+0.126}_{-0.098}$	$8.96^{+2.02}_{-1.65}$	$45.36^{+4.35}_{-4.21}$	$1.36^{+0.13}_{-0.12}$	$0.53^{+0.12}_{-0.09}$...
UGC 07866	P	-11.399	$0.205^{+0.107}_{-0.080}$	$4.58^{+0.23}_{-0.22}$	$47.67^{+4.69}_{-4.75}$	$1.35^{+0.13}_{-0.12}$	$0.53^{+0.13}_{-0.11}$...
UGC 08286	P	-11.135	$0.021^{+0.015}_{-0.014}$	$6.60^{+0.21}_{-0.20}$	$88.10^{+1.34}_{-2.07}$	$1.32^{+0.12}_{-0.11}$	$1.14^{+0.09}_{-0.08}$...
UGC 08490	P	-11.588	$0.035^{+0.015}_{-0.015}$	$5.20^{+0.47}_{-0.43}$	$55.39^{+2.58}_{-2.52}$	$1.37^{+0.13}_{-0.12}$	$0.67^{+0.11}_{-0.09}$...
UGC 08550	P	-11.388	$0.002^{+0.027}_{-0.026}$	$6.52^{+1.00}_{-0.86}$	$88.00^{+1.40}_{-2.17}$	$1.28^{+0.12}_{-0.11}$	$0.72^{+0.13}_{-0.11}$...
UGC 08699	P	-10.863	$-0.011^{+0.023}_{-0.024}$	$37.40^{+4.53}_{-4.04}$	$80.73^{+5.31}_{-5.93}$	$1.38^{+0.13}_{-0.12}$	$0.63^{+0.12}_{-0.10}$	$0.68^{+0.08}_{-0.07}$
UGC 08837	P	-11.286	$0.216^{+0.063}_{-0.049}$	$7.25^{+0.36}_{-0.34}$	$80.74^{+4.47}_{-4.70}$	$1.43^{+0.13}_{-0.12}$	$0.40^{+0.08}_{-0.07}$...
UGC 09037	P	-11.097	$-0.014^{+0.038}_{-0.037}$	$73.49^{+6.79}_{-6.18}$	$63.78^{+4.87}_{-4.74}$	$1.45^{+0.14}_{-0.13}$	$0.22^{+0.03}_{-0.03}$...
UGC 09133	P	-11.361	$0.042^{+0.007}_{-0.007}$	$35.41^{+3.58}_{-3.04}$	$64.78^{+4.59}_{-4.44}$	$1.50^{+0.15}_{-0.13}$	$0.83^{+0.09}_{-0.09}$	$0.72^{+0.04}_{-0.04}$
UGC 09992	C	-11.354	$0.361^{+0.098}_{-0.138}$	$9.52^{+2.53}_{-1.97}$	$35.87^{+6.37}_{-5.88}$	$1.34^{+0.13}_{-0.12}$	$0.50^{+0.12}_{-0.10}$...
UGC 10310	A	-11.125	$0.270^{+0.142}_{-0.136}$	$16.38^{+3.93}_{-3.31}$	$40.81^{+4.88}_{-4.78}$	$1.32^{+0.12}_{-0.11}$	$0.66^{+0.14}_{-0.12}$...
UGC 11455	P	-10.651	$-0.035^{+0.025}_{-0.028}$	$72.22^{+8.17}_{-7.36}$	$89.33^{+0.47}_{-0.73}$	$1.42^{+0.14}_{-0.12}$	$0.46^{+0.07}_{-0.06}$...
UGC 11557	C	-10.882	$0.360^{+0.101}_{-0.168}$	$18.22^{+4.20}_{-3.39}$	$34.01^{+5.91}_{-5.55}$	$1.40^{+0.13}_{-0.12}$	$0.35^{+0.09}_{-0.07}$...
UGC 11820	P	-11.301	$-0.015^{+0.019}_{-0.019}$	$12.15^{+3.03}_{-2.30}$	$44.21^{+6.75}_{-5.90}$	$1.20^{+0.11}_{-0.10}$	$0.98^{+0.15}_{-0.13}$...
UGC 11914	A	-9.760	$-0.448^{+0.057}_{-0.037}$	$9.50^{+1.32}_{-1.09}$	$49.36^{+3.64}_{-3.52}$	$1.42^{+0.14}_{-0.13}$	$0.27^{+0.04}_{-0.04}$	$0.81^{+0.06}_{-0.07}$
UGC 12506	P	-10.921	$0.214^{+0.050}_{-0.044}$	$117.01^{+10.55}_{-9.62}$	$86.11^{+2.48}_{-3.10}$	$1.43^{+0.14}_{-0.13}$	$1.04^{+0.13}_{-0.11}$...
UGC 12632	P	-11.405	$0.249^{+0.114}_{-0.085}$	$13.17^{+2.93}_{-2.49}$	$49.21^{+2.79}_{-2.77}$	$1.25^{+0.11}_{-0.11}$	$1.05^{+0.16}_{-0.14}$...
UGC 12732	P	-11.443	$0.124^{+0.077}_{-0.055}$	$13.11^{+3.32}_{-2.52}$	$48.12^{+4.98}_{-4.79}$	$1.26^{+0.12}_{-0.11}$	$0.86^{+0.12}_{-0.10}$...
UGCA 442	P	-11.393	$-0.051^{+0.012}_{-0.013}$	$4.20^{+0.21}_{-0.20}$	$51.12^{+3.93}_{-3.59}$	$1.29^{+0.12}_{-0.11}$	$0.45^{+0.11}_{-0.09}$...
UGCA 444	P	-11.550	$0.061^{+0.024}_{-0.022}$	$0.95^{+0.05}_{-0.05}$	$78.76^{+3.83}_{-3.88}$	$1.25^{+0.12}_{-0.11}$	$0.56^{+0.15}_{-0.12}$...

(This table is available in machine-readable form.)

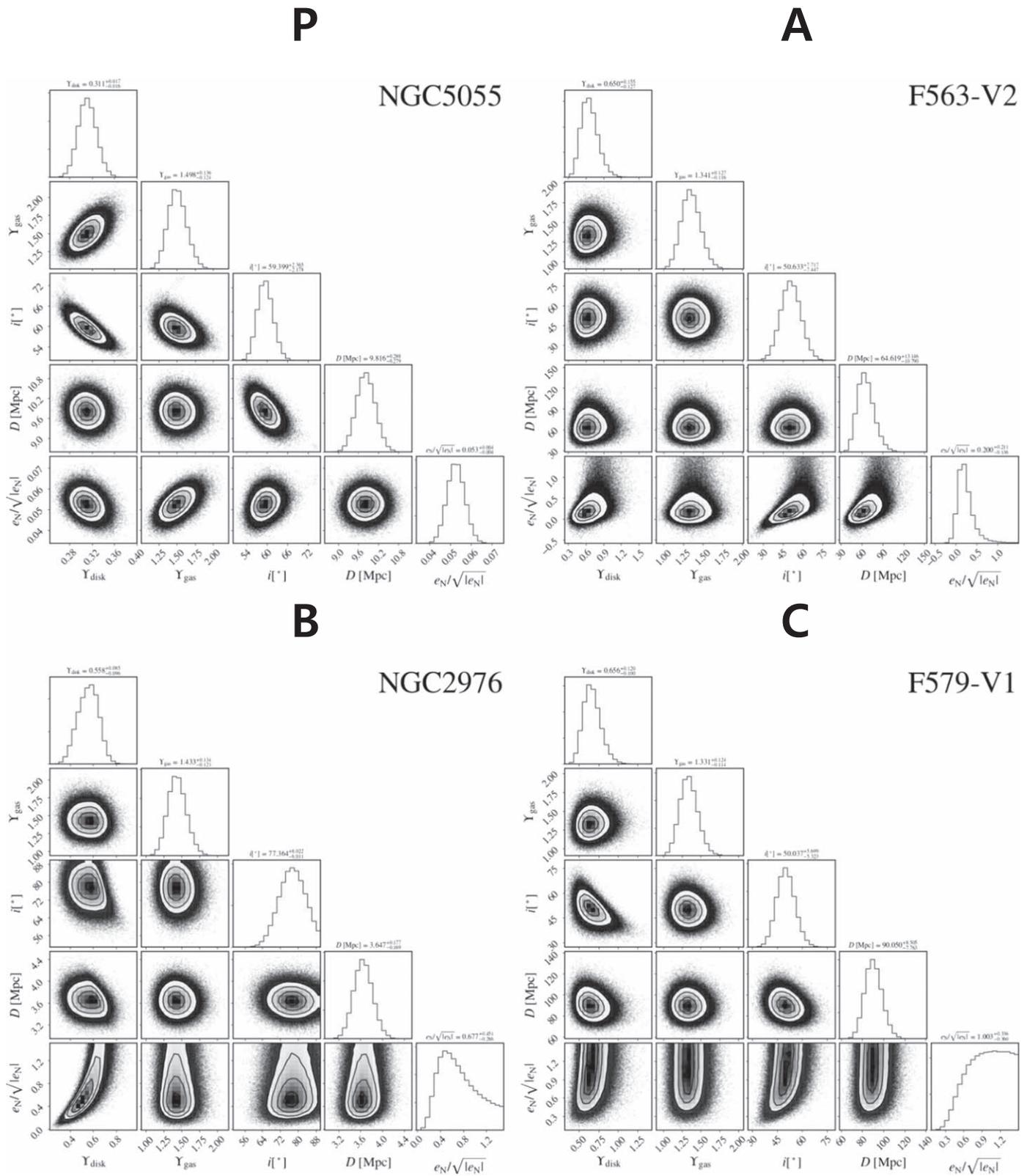


Figure 13. Examples showing the posterior pdf's of our model parameters for four types of pdf quality described in the text of the Appendix. For types A, B, and C, an extended prior range for $\tilde{\epsilon} \equiv e_N/\sqrt{|e_N|}$ is used to illustrate the behavior of its pdf. Thus, the values of $\tilde{\epsilon}$ for these cases are different from those given in Table 2.

Table 3
Newtonian Environmental Field Strength $\log(e_{N,env})$

Galaxy	Max Clustering	No Clustering
D512-2	-2.245 ± 0.261	-3.155 ± 0.285
D564-8	-2.283 ± 0.242	-3.178 ± 0.271
DDO 064	-2.257 ± 0.299	-3.162 ± 0.317
DDO 154	-2.166 ± 0.344	-3.052 ± 0.383
DDO 168	-2.194 ± 0.287	-3.081 ± 0.319
DDO 170	-1.915 ± 0.385	-2.825 ± 0.407
F563-1	-2.628 ± 0.127	-3.530 ± 0.138
F563-V1	-2.585 ± 0.139	-3.483 ± 0.126
F563-V2	-2.598 ± 0.110	-3.492 ± 0.115
F565-V2	-2.620 ± 0.124	-3.533 ± 0.126
F567-2	-2.505 ± 0.131	-3.412 ± 0.129
F568-1	-2.440 ± 0.134	-3.355 ± 0.128
F568-3	-2.459 ± 0.128	-3.368 ± 0.129
F568-V1	-2.380 ± 0.196	-3.289 ± 0.211
F571-8	-2.427 ± 0.240	-3.366 ± 0.259
F571-V1	-2.118 ± 0.340	-3.045 ± 0.340
F574-1	-2.217 ± 0.304	-3.169 ± 0.336
F574-2	-2.282 ± 0.417	-3.209 ± 0.441
F579-V1	-2.630 ± 0.207	-3.542 ± 0.218
IC 4202	-1.942 ± 0.438	-2.858 ± 0.479
NGC 0100	-2.667 ± 0.221	-3.561 ± 0.268
NGC 2683	-2.362 ± 0.252	-3.207 ± 0.381
NGC 2841	-2.395 ± 0.366	-3.288 ± 0.483
NGC 2903	-2.300 ± 0.243	-3.208 ± 0.257
NGC 2955	-2.520 ± 0.217	-3.425 ± 0.344
NGC 2998	-2.542 ± 0.222	-3.451 ± 0.258
NGC 3198	-2.335 ± 0.317	-3.248 ± 0.376
NGC 3726	-2.242 ± 0.340	-3.159 ± 0.369
NGC 3741	-2.307 ± 0.324	-3.195 ± 0.347
NGC 3769	-2.322 ± 0.279	-3.252 ± 0.311
NGC 3877	-2.331 ± 0.319	-3.266 ± 0.309
NGC 3893	-2.344 ± 0.304	-3.272 ± 0.316
NGC 3917	-2.396 ± 0.281	-3.325 ± 0.318
NGC 3949	-2.320 ± 0.324	-3.256 ± 0.331
NGC 3953	-2.382 ± 0.304	-3.306 ± 0.323
NGC 3972	-2.333 ± 0.321	-3.268 ± 0.316
NGC 3992	-2.540 ± 0.192	-3.479 ± 0.209
NGC 4010	-2.307 ± 0.342	-3.242 ± 0.318
NGC 4013	-2.215 ± 0.274	-3.142 ± 0.290
NGC 4051	-2.271 ± 0.288	-3.196 ± 0.346
NGC 4068	-2.272 ± 0.315	-3.157 ± 0.356
NGC 4085	-2.253 ± 0.353	-3.196 ± 0.348
NGC 4088	-2.235 ± 0.351	-3.175 ± 0.353
NGC 4100	-2.382 ± 0.337	-3.322 ± 0.344
NGC 4138	-2.278 ± 0.336	-3.218 ± 0.313
NGC 4157	-2.266 ± 0.341	-3.207 ± 0.286
NGC 4183	-2.280 ± 0.302	-3.217 ± 0.324
NGC 4214	-2.263 ± 0.340	-3.149 ± 0.365
NGC 4217	-2.285 ± 0.262	-3.213 ± 0.278
NGC 4389	-2.316 ± 0.288	-3.243 ± 0.306
NGC 4559	-2.036 ± 0.445	-2.938 ± 0.474
NGC 5005	-2.132 ± 0.334	-3.032 ± 0.404
NGC 5033	-2.381 ± 0.272	-3.324 ± 0.277
NGC 5055	-2.155 ± 0.314	-3.064 ± 0.339
NGC 5371	-2.268 ± 0.249	-3.191 ± 0.263
NGC 5585	-2.264 ± 0.269	-3.149 ± 0.290
NGC 5907	-2.395 ± 0.193	-3.322 ± 0.203
NGC 7814	-2.670 ± 0.307	-3.560 ± 0.408
PGC 51017	-2.261 ± 0.259	-3.172 ± 0.270
UGC 00191	-2.713 ± 0.201	-3.620 ± 0.233
UGC 00634	-2.714 ± 0.199	-3.623 ± 0.249
UGC 00891	-2.590 ± 0.201	-3.487 ± 0.217
UGC 04499	-2.470 ± 0.265	-3.391 ± 0.280
UGC 05005	-2.619 ± 0.141	-3.522 ± 0.142
UGC 05414	-2.277 ± 0.287	-3.187 ± 0.307

Table 3
(Continued)

Galaxy	Max Clustering	No Clustering
UGC 05716	-2.378 ± 0.235	-3.303 ± 0.252
UGC 05721	-2.126 ± 0.304	-3.030 ± 0.347
UGC 05750	-2.561 ± 0.163	-3.468 ± 0.169
UGC 05764	-2.232 ± 0.261	-3.149 ± 0.286
UGC 05829	-2.189 ± 0.324	-3.091 ± 0.344
UGC 05986	-2.163 ± 0.348	-3.087 ± 0.342
UGC 05999	-2.601 ± 0.160	-3.512 ± 0.184
UGC 06399	-2.412 ± 0.233	-3.337 ± 0.263
UGC 06446	-2.394 ± 0.240	-3.327 ± 0.265
UGC 06614	-2.011 ± 0.426	-2.954 ± 0.433
UGC 06628	-2.291 ± 0.324	-3.217 ± 0.313
UGC 06667	-2.322 ± 0.286	-3.248 ± 0.290
UGC 06786	-2.649 ± 0.165	-3.587 ± 0.181
UGC 06787	-2.416 ± 0.337	-3.353 ± 0.374
UGC 06818	-2.289 ± 0.282	-3.209 ± 0.299
UGC 06917	-2.364 ± 0.276	-3.300 ± 0.288
UGC 06923	-2.359 ± 0.252	-3.294 ± 0.271
UGC 06930	-2.377 ± 0.282	-3.314 ± 0.277
UGC 06973	-2.286 ± 0.312	-3.215 ± 0.315
UGC 06983	-2.414 ± 0.273	-3.361 ± 0.271
UGC 07089	-2.234 ± 0.326	-3.160 ± 0.356
UGC 07125	-2.117 ± 0.330	-3.031 ± 0.348
UGC 07151	-2.081 ± 0.282	-2.965 ± 0.321
UGC 07232	-2.202 ± 0.344	-3.090 ± 0.360
UGC 07261	-1.741 ± 0.478	-2.650 ± 0.513
UGC 07323	-2.164 ± 0.333	-3.065 ± 0.349
UGC 07399	-2.236 ± 0.317	-3.165 ± 0.304
UGC 07524	-2.210 ± 0.384	-3.088 ± 0.445
UGC 07559	-2.228 ± 0.381	-3.107 ± 0.430
UGC 07577	-2.301 ± 0.319	-3.192 ± 0.341
UGC 07603	-2.145 ± 0.392	-3.030 ± 0.446
UGC 07608	-2.172 ± 0.334	-3.078 ± 0.366
UGC 07690	-2.143 ± 0.332	-3.043 ± 0.368
UGC 07866	-2.299 ± 0.402	-3.187 ± 0.427
UGC 08286	-2.173 ± 0.307	-3.071 ± 0.337
UGC 08490	-2.270 ± 0.272	-3.147 ± 0.343
UGC 08550	-2.125 ± 0.321	-3.014 ± 0.349
UGC 08699	-2.579 ± 0.313	-3.524 ± 0.265
UGC 08837	-2.108 ± 0.260	-3.004 ± 0.289
UGC 09037	-2.719 ± 0.251	-3.603 ± 0.282
UGC 09133	-2.676 ± 0.212	-3.603 ± 0.241
UGC 12506	-2.567 ± 0.259	-3.511 ± 0.272
UGC 12732	-2.667 ± 0.243	-3.577 ± 0.258
UGC A281	-2.206 ± 0.303	-3.097 ± 0.329

(This table is available in machine-readable form.)

ORCID iDs

Kyu-Hyun Chae  <https://orcid.org/0000-0002-6016-2736>
Harry Desmond  <https://orcid.org/0000-0003-0685-9791>
Federico Lelli  <https://orcid.org/0000-0002-9024-9883>
Stacy S. McGaugh  <https://orcid.org/0000-0002-9762-0980>
James M. Schombert  <https://orcid.org/0000-0003-2022-1911>

References

Angus, G. W., Famaey, B., & Buote, D. A. 2008, *MNRAS*, **387**, 1470
Asencio, E., Banik, I., & Kroupa, P. 2021, *MNRAS*, **500**, 5249
Babyk, I. V., McNamara, B. R., Nulsen, P. E. J., et al. 2018, *ApJ*, **857**, 32
Banik, I., Thies, I., Famaey, B., et al. 2020, *ApJ*, **905**, 135
Bekenstein, J., & Milgrom, M. 1984, *ApJ*, **286**, 7
Bernardi, M., Meert, A., Sheth, R. K., et al. 2013, *MNRAS*, **436**, 697

- Brada, R., & Milgrom, M. 2000, *ApJL*, **531**, 21L
- Bullock, J. S., & Boylan-Kolchin, M. 2017, *ARA&A*, **55**, 343
- Chae, K.-H., Bernardi, M., Domínguez Sánchez, H., & Sheth, R. K. 2020a, *ApJL*, **903**, L31
- Chae, K.-H., Bernardi, M., Sheth, R. K., & Gong, I.-T. 2019, *ApJ*, **877**, 18
- Chae, K.-H., Lelli, F., Desmond, H., et al. 2020b, *ApJ*, **904**, 51, (Paper I)
- Chae, K.-H., Lelli, F., Desmond, H., et al. 2021, *ApJ*, **910**, 81
- Cooke, R. J., Pettini, M., & Steidel, C. C. 2018, *ApJ*, **855**, 102
- Das, S., Mathur, S., Gupta, A., et al. 2019, *ApJ*, **887**, 257
- Das, S., Mathur, S., & Gupta, A. 2020, *ApJ*, **897**, 63
- Ettori, S., Ghirardini, V., Eckert, D., et al. 2019, *A&A*, **621**, A39
- Famaey, B., & Binney, J. 2005, *MNRAS*, **363**, 603
- Famaey, B., & McGaugh, S. S. 2012, *LRR*, **15**, 10
- Famaey, B., McGaugh, S., & Milgrom, M. 2018, *MNRAS*, **480**, 473
- Geller, M. J., & Huchra, J. P. 1989, *Sci*, **246**, 879
- Górski, K. M., Hivon, E., Banday, A. J., et al. 2005, *ApJ*, **622**, 759
- Haghi, H., Bazkiaei, A. E., Zonoozi, A. H., & Kroupa, P. 2016, *MNRAS*, **458**, 4172
- Haghi, H., Kroupa, P., Banik, I., et al. 2019, *MNRAS*, **487**, 2441
- Haslbauer, M., Banik, I., & Kroupa, P. 2020, *MNRAS*, **499**, 2845
- Hees, A., Famaey, B., Angus, G. W., & Gentile, G. 2016, *MNRAS*, **455**, 449
- Henriques, B. M. B., White, S. D. M., Thomas, P. A., et al. 2015, *MNRAS*, **451**, 2663
- Joeveer, M., & Einasto, J. 1978, in *IAU Symp. 79, The Large Scale Structure of the Universe*, ed. M. S. Longair & J. Einasto (Dordrecht: Reidel Publishing), 241
- Karachentsev, I. D., & Kaisina, E. I. 2019, *AstBu*, **74**, 111
- Karachentsev, I. D., Kaisina, E. I., & Makarov, D. I. 2018, *MNRAS*, **479**, 4136
- Kroupa, P. 2012, *PASA*, **29**, 395
- Lavaux, G., & Hudson, M. J. 2011, *MNRAS*, **416**, 2840
- Lelli, F., McGaugh, S. S., & Schombert, J. M. 2016, *AJ*, **152**, 157
- Lelli, F., McGaugh, S. S., Schombert, J. M., & Pawlowski, M. S. 2017, *ApJ*, **836**, 152
- Li, P., Lelli, F., McGaugh, S., & Schombert, J. 2018, *A&A*, **615**, 70
- Li, P., Lelli, F., McGaugh, S., & Schombert, J. 2020, *ApJS*, **247**, 31
- Li, P., Lelli, F., McGaugh, S., Schombert, J., & Chae, K.-H. 2021, *A&A*, **646**, L13
- Li, C., & White, S. D. M. 2009, *MNRAS*, **398**, 2177
- Lim, S. H., Mo, H. J., Wang, H., et al. 2020, *ApJ*, **889**, 48
- Macquart, J.-P., Prochaska, J. X., McQuinn, M., et al. 2020, *Natur*, **581**, 391
- Mantz, A. B., Allen, S. W., Morris, R. G., et al. 2016, *MNRAS*, **463**, 3582
- McGaugh, S. S. 2015, *CaJPH*, **93**, 250
- McGaugh, S. S., Lelli, F., & Schombert, J. M. 2016, *PhRvL*, **117**, 201101
- McGaugh, S. S., Lelli, F., & Schombert, J. M. 2020, *RNAAS*, **4**, 45
- McGaugh, S., & Milgrom, M. 2013a, *ApJ*, **766**, 22
- McGaugh, S., & Milgrom, M. 2013b, *ApJ*, **775**, 139
- McGaugh, S. S., & Schombert, J. M. 2014, *AJ*, **148**, 77
- Milgrom, M. 1983, *ApJ*, **270**, 365
- Milgrom, M. 2008, *NewAR*, **51**, 906
- Milgrom, M. 2010, *MNRAS*, **403**, 886
- Milgrom, M. 2014, *SchpJ*, **9**, 31410
- Moffett, A. J., Ingarfield, S. A., Driver, S. P., et al. 2016, *MNRAS*, **457**, 1308
- Nicastro, F., Kaastra, J., Krongold, Y., et al. 2018, *Natur*, **558**, 406
- Noordermeer, E., van der Hulst, J. M., Sancisi, R., Swaters, R. S., & van Albada, T. S. 2007, *MNRAS*, **376**, 1513
- Piffaretti, R., Arnaud, M., Pratt, G. W., et al. 2011, *A&A*, **534**, A109
- Sanders, R. H. 1999, *ApJL*, **512**, L23
- Sancisi, R., Fraternali, F., Oosterloo, T., & van der Hulst, T. 2008, *A&ARv*, **15**, 189
- Schombert, J., McGaugh, S., & Lelli, F. 2019, *MNRAS*, **483**, 1496
- Shull, J. M., Smith, B. D., & Danforth, C. W. 2018, *ApJ*, **759**, 23
- Skordis, C., & Zlošnik, T. 2021, *PhRvL*, **127**, 161302
- Stiskalek, R., Desmond, H., Holvey, T., et al. 2021, *MNRAS*, **506**, 3205
- Tully, R. B., Pomarède, D., Graziani, R., et al. 2019, *ApJ*, **880**, 24
- Voges, W., Aschenbach, B., Boller, T., et al. 1999, *A&A*, **349**, 389
- Will, C. M. 2014, *LRR*, **17**, 4
- Wu, X., & Kroupa, P. 2015, *MNRAS*, **446**, 330
- Zhang, Y.-Y., Andernach, H., Caretta, C. A., et al. 2011, *A&A*, **526**, A105